Curcumin derivatives and Aβ-fibrillar aggregates: an interactions' study for diagnostic/therapeutic purposes in neurodegenerative diseases.

Giulia Orteca,[a] Francesco Tavanti,[a] Zuzana Bednarikova,[b] Zuzana Gazova,[b] Giovanna Rigillo,[c] Carol Imbriano,[c] Valentina Basile,[c] Mattia Asti,[d] Luca Rigamonti,[a] Monica Saladini,[a] Erika Ferrari,[a,*] and Maria Cristina Menziani[a]

[a] Department of Chemical and Geological Sciences, University of Modena and Reggio Emilia, via G. Campi 103, 41125 Modena, Italy.

[b] Department of Biophysics, Institute of Experimental Physics, Slovak Academy of Sciences, Watsonova 47, 040 01 Kosice, Slovakia.

[c] Department of Life Sciences, University of Modena and Reggio Emilia, via G. Campi 213/D, 41125 Modena, Italy.

[d] Nuclear Medicine Unit - Advanced Technology Department, AUSL – IRCCS Reggio Emilia, viale Amendola 2, 42122 Reggio Emilia, Italy.

* Corresponding author: Department of Chemical and Geological Sciences, University of Modena and Reggio Emilia. *E-mail address*: erika.ferrari@unimore.it, tel. +39 0592058631 (E. Ferrari)

ABSTRACT

Several neurodegenerative diseases, like Alzheimer's (AD), are characterized by amyloid fibrillar deposition of misfolded proteins, and this feature can be exploited for both diagnosis and therapy design. In this paper, structural modifications of curcumin scaffold were examined in order to improve its bioavailability and stability in physiological conditions, as well as its ability to interfere with β-amyloid fibrils and aggregates. The acid-base behaviour of curcumin derivatives, their pharmacokinetic stability in physiological conditions, and *in vitro* ability to interfere with Aβ fibrils at different incubation time were investigated. The mechanisms governing these phenomena have been studied at atomic level by means of molecular docking and dynamic simulations. Finally, biological activity of selected curcuminoids has been investigated *in vitro* to evaluate their safety and efficiency in oxidative stress protection on hippocampal HT-22 mouse cells.

Two aromatic rings, π-conjugated structure and H-donor/acceptor substituents on the aromatic rings showed to be the *sine qua non* structural features to provide interaction and disaggregation activity even at very low incubation time (2 h). Computational simulations proved that upon binding the ligands modify the conformational dynamics and/or interact with the amyloidogenic region of the protofibril facilitating disaggregation. Significantly, *in vitro* results on hippocampal cells pointed out protection against glutamate toxicity and safety when administered at low concentrations (1 μM). On the overall, in view of its higher stability in physiological conditions with respect to curcumin, of his rapid binding to fibrillar aggregates and strong depolymerizing activity, phtalimmide derivative **K2F21** appeared a good candidate for both AD diagnostic and therapeutic purposes.

KEYWORDS: Amyloid β fibrillar aggregates; Alzheimer's Disease; curcumin-derivatives; Molecular Dynamics simulations; hippocampal HT-22 mouse cells.

1. INTRODUCTION

The amyloid deposition of misfolded proteins, such as hyperphosphorylated tau, amyloid β (Aβ) peptide, or α-synuclein, has been recognized as a feature of many neurodegenerative diseases (NDD) [1]. In fact, the degree of abnormal protein deposition commonly correlates with the clinical progression and severity of the pathology [1]. In addition to the accepted role of amyloid plaques in Alzheimer's disease (AD) pathogenesis, amyloid deposition plays a key contribution in cognitive impairments associated to synucleinopathies, such as Parkinson's disease (PD), related Parkinson's disease with dementia (hPDD) and dementia with Lewy bodies (DLB) [2]. Monomeric Aβ peptides normally present in the human brain have no deleterious effects on neurons. However, they have a tendency to self- assembly into amyloid aggregates from which the oligomeric species are most likely responsible for the pathogenesis of AD and cerebral amyloid angiopathy (CAA) [3].

The amyloid accumulation of Aβ peptides has a crucial role in neuronal dysfunction, eventually leading to cell death. Indeed, apoptosis occurs and contributes to AD onset and progression [4]. Several stimuli trigger the apoptotic events, i.e. oxidative stress, endoplasmic reticulum stress, metabolic dysfunction, DNA damage and reduced levels of anti-apoptotic genes [4–6]. In particular, oxidative stress has a pivotal role in the AD pathophysiology: reactive oxygen species (ROS) in association with nitrogen species (RNS), precede the formation of senile plaques [7]. The vicious circle, existing between ROS produced by damaged mitochondria during oxidative stress and Aβ peptides' accumulation, accelerates AD progression [8]. Moreover, the oxidative stress, together with the deposition of Aβ in senile plaques and chronically increased concentrations of glutamate, trigger an increase in the activity of the glutamatergic system, which finally leads to neuronal dysfunction and cell death in AD [9].

Shading light on the mechanisms of amyloid fibril formation and disaggregation paves the way to several strategies to mitigate AD that remains an extremely challenging ailment to defeat, as recently pinpointed by Doig *et al.* [10]. Drugs under investigation comprise antibody-based immunotherapeutics such as aducanumab, peptidomimetics, glutamatergic system targeting molecules (memantine), and natural occurring small-molecules [11,12]. Antioxidants based on polyphenols, among them epigallo catechin gallate (EGCG), resveratrol and curcumin, have a demonstrated protecting activity against Aβ-induced neurotoxicity [13] with the advantage of being naturally occurring and non-toxic at reasonable concentration [14,15].

Planar molecules, such as Congo Red, chrysamine G and curcumin [16,17], demonstrated to have high affinity for Aβ amyloid aggregates, hence they could be used as diagnostic tools for detection of amyloid aggregation at early stages of the disease [18,19]. Whereas the importance of specific amino acid residues in the recognition process has been recently highlighted [20], the

structures of fibrils and oligomers, the precise location of ligand binding sites and the mechanisms of fibril destabilization upon ligand interaction with small molecules still remain largely obscure and few studies are reported [21]. Computational simulations have been recently used to complement experimental studies in the elucidation of curcumin binding modes and functionalities [22–24].

In particular, *in silico* studies highlighted the existence of several putative non-overlapping binding sites of the full-length Aβ models for curcumin [25–29]. Moreover, based on molecular dynamics (MD) simulation studies, protofibril distortion upon curcumin interaction has been identified as the main cause for prevention of oligomerization by perturbation of Aβ aggregation pathway and the formation of nontoxic aggregates [25,30].

Despite Curcumin (**C21**) possesses pleiotropic activities of considerable benefit, its use in clinical applications is limited by low bioavailability, instability and poor water solubility, as recently pinpointed by Nelson *et al.* [31]. Several articles about effect of modified curcumin on Aβ amyloid aggregation has been published recently [32,33], however new scaffold modifications that may turn curcumin into stable, safe, and potent ligand for fibrillar aggregates still need to be explored.

In the present study, structural modifications of curcumin scaffold were examined in order to improve its bioavailability and possibly the ability to interfere with β-amyloid fibrils and aggregates. In particular, since tautomeric equilibrium is supposed to play a key role in curcumin instability, the replacement of the 1,3-dicarbonilic portion with isosteres is a promising strategy. The functionalization of β-diketo moiety was carried out by the insertion of phthalimide-functionalized chain in α position to the two carbonyl groups (K series), consistently to previously synthesized KT series that demonstrated improved stability with respect to the lead compound [34]. Finally, the removal of keto-enol moiety in favor of a pyrazole ring (P series) allows to stiffen the structure and favor π conjugation, features that might improve both stability and interaction with Aβ aggregates, as previously reported for other heterocyclic curcumin analogs [33].

The new derivatives (**Figure 1)** have been characterized in depth in relation to acid-base behaviour and pharmacokinetic stability in physiological conditions, and tested for their *in vitro* ability to interfere with Aβ fibrils at different incubation time so to inspect their potential applications for therapy as well as for AD early diagnosis. The mechanisms governing these phenomena have been studied at atomic level by means of molecular docking and dynamic simulations. Finally, biological activity of selected curcuminoids has been investigated *in vitro* to evaluate their safety and efficiency in oxidative stress protection on neuronal cells.

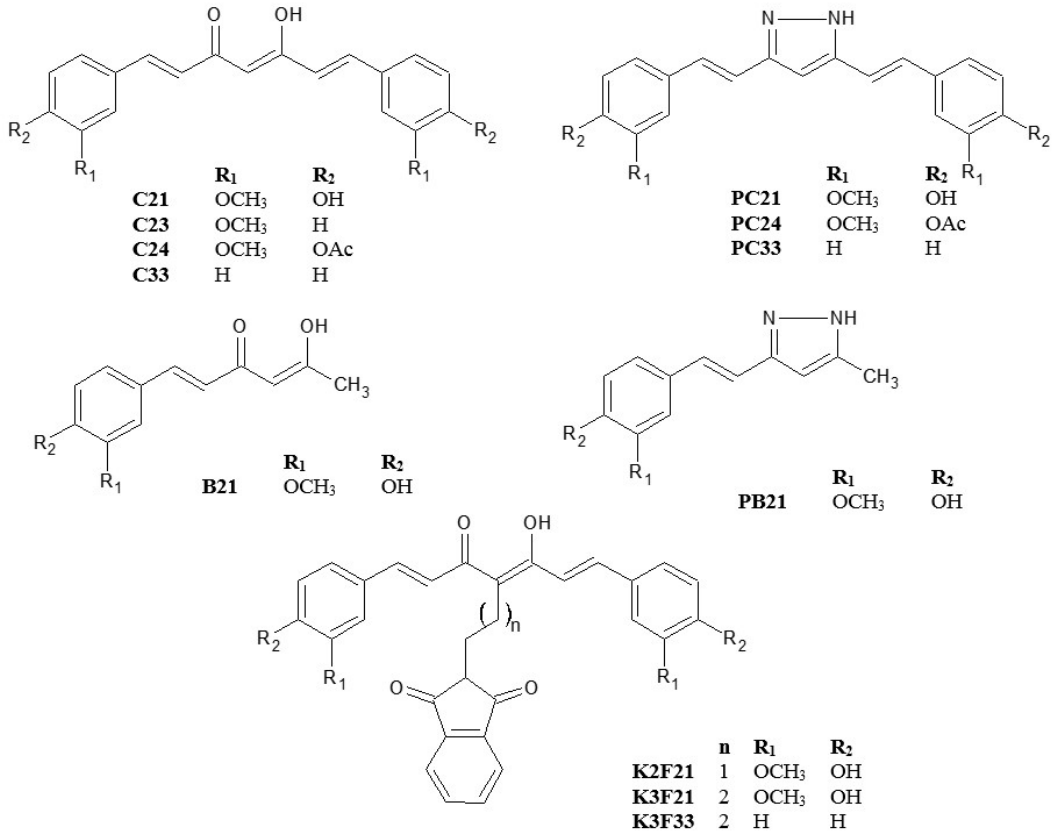

Figure 1. Chemical structure of investigated curcuminoids.

2. RESULTS AND DISCUSSION

2.1 Chemistry.

All curcumin-like compounds were synthesized according to one-pot "Pabon reaction" [35] or its modifications [36], in order to gain derivatives reported in **Figure 1**. In solution, all the compounds gifted with the β-diketo moiety, namely C and K serie, show tautomerism between diketo (DK) and keto-enol (KE) forms, that typically display two main UV-vis absorption bands at 350–370 nm and 400–430 nm, respectively [37,38]. The P series, in which the addition of pyrazole ring is aimed to rise molecular planarity and stability, is characterized by only one main absorption band around 340 nm (**Figure 1 SI**).

Since acid/base behaviour may strongly affect drug uptake, distribution and interaction with biological targets, the evaluation of overall protonation constants and species distribution curves have a key role in the development of pharmaceuticals. The overall protonation constants (**Table 1 SI**) were refined from spectrophotometric data with HypSpec Software [39,40]. For **B21** and **K2F21** (**Figure 2**), as pH is increased from 5 to 11, an isosbestic point appears at about 375 nm, hinting the equilibrium between neutral and dissociated forms around pH 8.5/9. All C and K compounds display

a keto-enol dissociation constant around 8.5, followed by the deprotonation of phenols at pH 9-11. As previously observed for curcumin analogs [34,41], the length of alkyl spacer in K series does not impact significantly the acidity of keto-enol moiety, hence we may predict that acid-base properties of **K2F21** and **K3F21** should overlap.

For **PC21,** a first deprotonation is observed at very acid pH (~2), due to the dissociation of pyrazolidinium cation to give the neutral form of pyrazole, followed by the deprotonation of the two phenolic groups at pH 8.5-9 (**Figure 1 SI**).

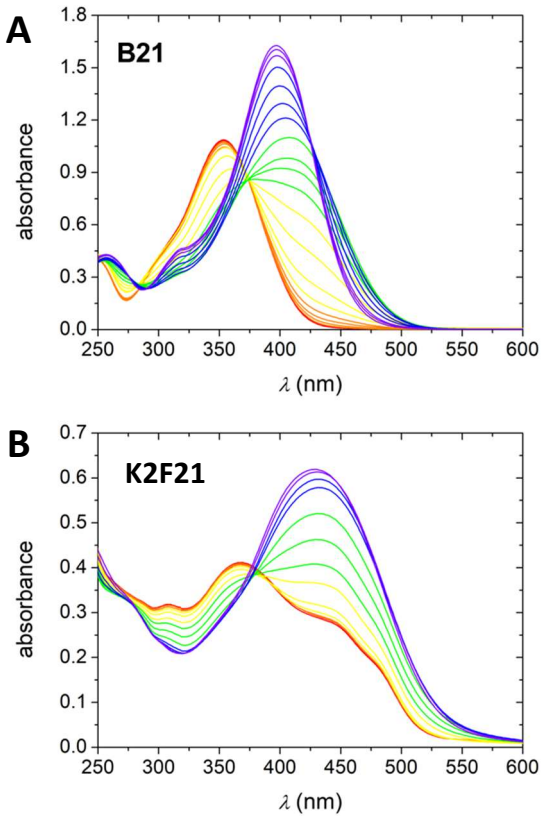

Figure 2. pH-metric spectrophotometric titration of **B21** (A) and **K2F21** (B) in aqueous medium at 298 K in the 250–600 nm spectral range, pH starting from 5 (red) to 11.0 (violet).

Lipophilicity is of utmost importance in view of uptake and distribution in biological systems. Particularly when non-specific mechanisms take place, neutral species with low molecular weight (< 600 Da) are commonly better internalized than charged molecules. All the investigated compounds are mainly in the neutral form in physiological conditions (pH 7.4, **Figure 2 SI**), especially, **K2F21** is almost completely undissociated, suggesting a shift in favour of the diketo form and a decrease in keto-enol acidity compared to C compounds, driven by the addition of the alkyl chain to the keto-enol moiety.

With respect to the lead curcumin, K and P type of compounds showed an improved stability in physiological conditions (**Figure 3 SI**), with a residual percentage (%) within the first 2 hours close

to 60 % and 25 % for P series and K series, respectively. The residual % was estimated as $A_t \cdot 100/A_0$, where A_t and A_0 stand for absorbance at λ_{max} at *time t* and *time zero,* respectively.

2.2 ***Interference of curcumin derivatives with Aβ$_{1-40}$ amyloid fibrils in vitro.***

All derivatives were screened for their ability to interfere with Aβ$_{1-40}$ amyloid fibrils. Initially we investigated the interaction of 10 μM solution of each derivative with equimolar amounts of Aβ$_{1-40}$ fibrils using the Thioflavin T (ThT) fluorescence assay. The fluorescence intensities observed for fibrils after 24 h incubation with all derivatives (normalized to the fluorescence signal observed for fibrils alone (AF)) are shown in **Figure 3A**. The decrease in fluorescence intensity corresponds to the efficiency of derivatives to destroy the fibrils.

Addition of derivatives to Aβ$_{1-40}$ amyloid fibrils led to different effects depending on their structure. Significant fluorescence decrease, corresponding to binding of compounds to fibrils and subsequent fibril disruption, was observed for derivatives with vanillin-like aromatic structure (**C21**, **K2F21**, **K3F21**, **PC21** and **PC24**). The fluorescence intensities are lower than 25% of fluorescence signal observed for untreated fibrils, indicating higher than 75% destroying efficacy. On the other hand, weak destroying activity was observed for derivatives from each series that have no substituent on the aromatic rings ($R_1 = R_2 = H$), i.e. **C33**, **K3F33** and **PC33**. The fluorescence intensities observed for fibrils in presence of these derivatives were comparable or only slightly lower than signal detected for fibrils alone. A similar negligible destroying effect was determined for derivatives **PB21** and **B21**. In order to compare the ability to destroy Aβ$_{1-40}$ amyloid fibrils, the DC_{50} values (compound concentration at which 50 % of fibrils are destroyed) were determined using ThT assay. ThT fluorescence intensities of 10 μM solution of fibrils after 24 h incubation with curcumins at concentrations ranging from 100 pM to 1 mM were measured and data for selected derivatives are shown in **Figure 3B-D**. The DC_{50} values calculated for all studied compounds are reported in **Table 1**.

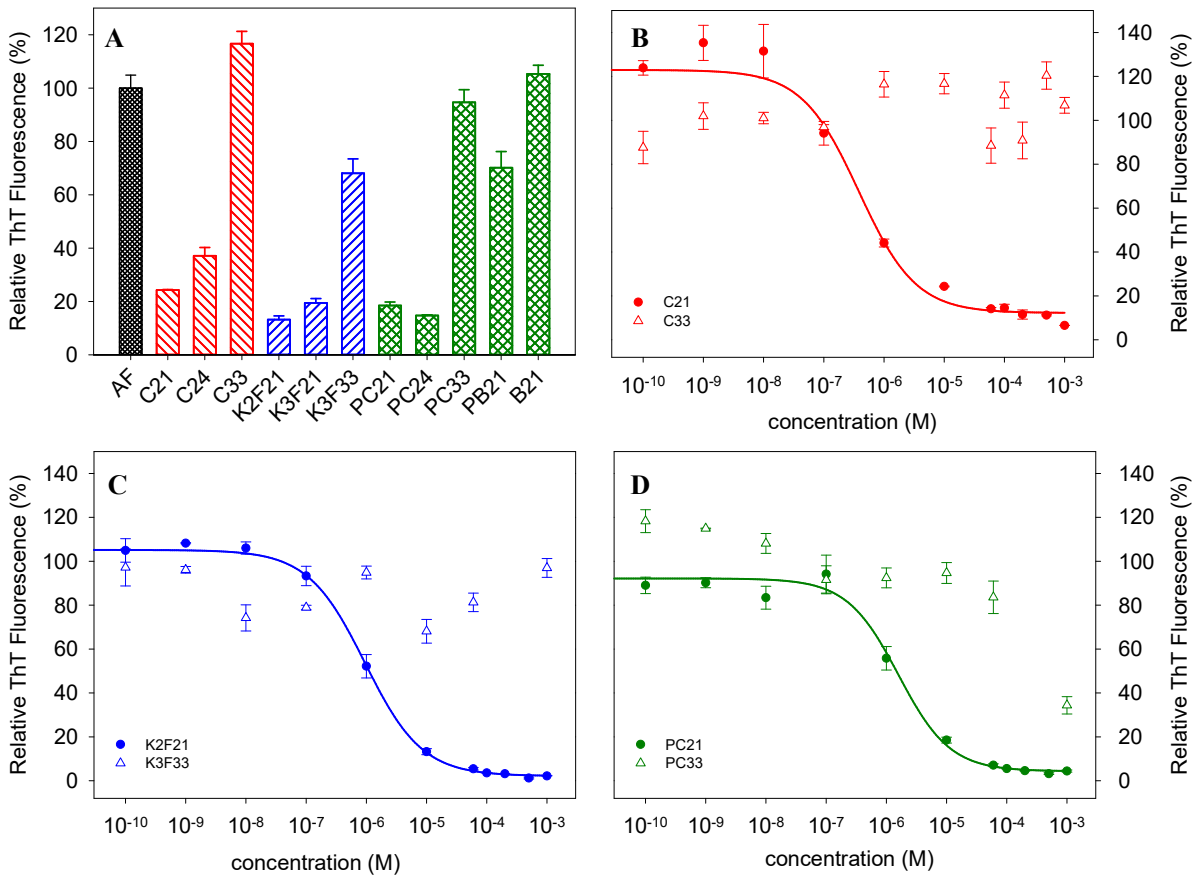

Figure 3. A) ThT fluorescence intensities of 10 μM $A\beta_{1-40}$ fibrils alone (AF) and after 24 h treatment with 10 μM curcuminoid derivatives. **B - D**) The effect of increasing curcumin derivative concentration on 10 μM $A\beta_{1-40}$ fibrils detected using ThT assay: **B**) Curcumin (red circles), **C33** (empty red triangles); **C**) **K2F21** (blue circles), **K3F33** (empty blue triangles); **D**) **PC21** (green circles), **PC33** (empty green triangles). The average fluorescence values were fitted by a nonlinear least-square methods using SigmaPlot software and used for calculation of DC_{50} values. The fluorescence intensities were normalized to the fluorescence intensities observed for fibrils in the absence of derivatives (taken as 100%). The error bars represent the average deviation for measurements of fluorescence intensities of three replicates.

It is evident that the studied compounds have a different impact on $A\beta_{1-40}$ amyloid fibrils, in particular the aromatic substituents rather than the central moiety (β-diketo/pyrazole) seems to drive the interaction with fibrils. Indeed, derivatives with no substituents on aromatic ring (i.e.**C33**, **K3F33**, **PC33**) have not noteworthy effect on amyloid fibrils (**Figure 3,** empty triangles), while the substituted ones favor disaggregation as shown by the fluorescence decrease that is dose-dependent (**Figure 3**, full circles) and allows to calculate DC_{50} values (**Table 1**).

Table 1. DC_{50} values observed for studied curcumin derivatives after 24 h (*) and 2 h (**) incubation by Thioflavin T assay. (N/A - not available due to very weak depolymerizing activity.)

Compound	DC_{50} (μM)*	DC_{50} (μM)**
C21	0.78 ± 0.04	0.73 ± 0.07
C24	1.95 ± 0.54	1.0 ± 0.05
C23	N/A	
C33	N/A	
K2F21	1.11 ± 0.23	0.14 ± 0.02
K3F21	1.16 ± 0.18	
K3F33	N/A	
PC21	1.47 ± 0.37	
PC24	0.31 ± 0.01	0.65 ± 0.03
PC33	N/A	
PB21	38.8 ± 5.67	
B21	N/A	

Derivatives with the aromatic structure of vanillin (R_1 = OCH_3 and R_2 = OH/AcO), especially **PC24** and **C21,** showed the highest destroying effect, consistently with their lowest DC_{50} values. Comparing **PC21** (1.47 μM) and **PB21** (38.8 μM), it is clear the need of a highly conjugated structure with π delocalized electrons. For **K** series, there is no major effect given by the length of the spacer in K series, and in general, all K derivatives showed a slightly lower activity compared to **C21**. These results are in great agreement with comprehensive study about structure-activity relationship of different curcumin derivatives done by Reinke and co-workers [16]. They have shown that the important features for activity of curcumin-based Aβ fibril ligands are: i) presence of both aromatic rings; ii) connection by rigid linker with a length of 8 - 16 Å; iii) hydroxyl or other polar substituents on the peripheral aromatic groups. Accordingly, top lead derivatives (**C21**, **C24**, **K2F21,** and **PC24**) satisfy all these criteria.

Furthermore, it was recently demonstrated that gallium-68 curcuminoids are able to bind $Aβ_{1–40}$ aggregates after 3 h incubation suggesting their potential applications as diagnostic tools for fibrils targeting using PET imaging technique [42,43]. Consequently, in order to evaluate the possibility to employ these derivatives for diagnostic purposes, we tested the activity of top lead compounds after 2 h incubation with $Aβ_{1-40}$ fibrils. As it is evident from **Table 1**, DC_{50} values after 2h incubation are similar or even one order of magnitude lower (**K2F21)** than DC_{50} values after 24 h incubation, hinting

a rapid binding to fibrillar aggregates and strong depolymerizing activity, with the strongest activity provided by **K2F21**.

Atomic force microscopy (AFM) can be exploited to confirm ThT results and visualize the drug effect on amyloid fibrils, Indeed, $A\beta_{1-40}$ fibrils (control - untreated sample) have a typical unbranched, linear amyloid morphology (**Figure 4A**) that becomes less dense and shortens upon 24 h incubation with **K2F21** and **C21** (**Figure 4C and D**), confirming their strong interaction and destroying propensity. Unsubstituted compounds, like **C33**, don't spoil fibrillar aggregates (**Figure 4B**), confirming ThT assay inactivity.

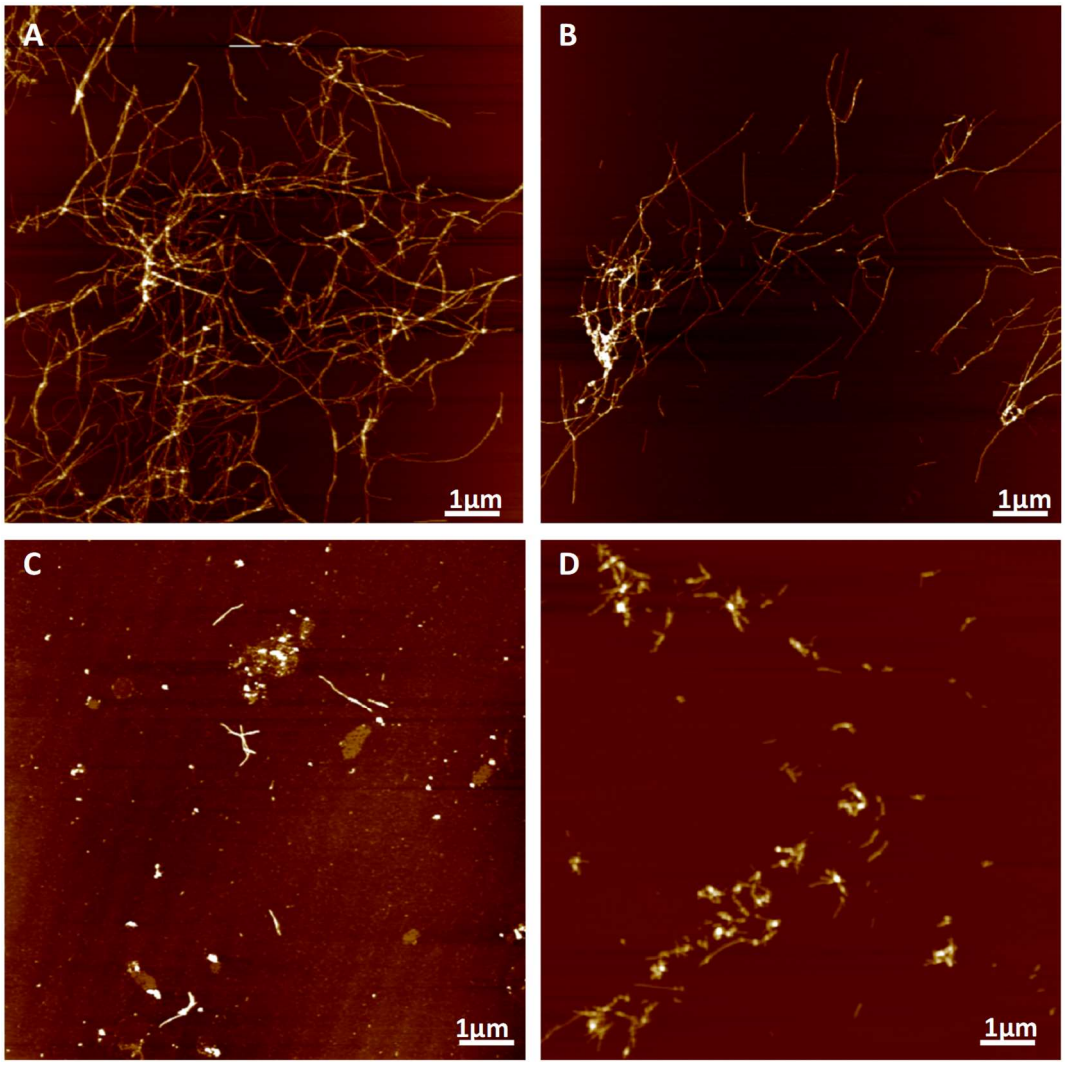

Figure 4. AFM images of 10 µM $A\beta_{1-40}$ fibrils alone (**A**) and after 24 h treatment with 10 µM curcumin derivatives with different extent of destroying activities: **C33** (**B**), **K2F21** (**C**) and **C21** (**D**).

2.3. Atomic description of the binding to the Aβ$_{1-40}$ protofibrils by selected curcuminoids.

In order to investigate at atomic details the perturbations induced by curcuminoids binding to the $A\beta_{1-40}$ preformed fibrils, MD simulations have been carried out on representative compounds of the three investigated series (C, P, K), that exhibited high affinity for $A\beta_{1-40}$ fibril aggregates by ThT

assay, namely **C21**, **PC24**, and **K2F21**. The ligand putative binding sites were identified by means of docking experiments to a protofibril formed by ten $A\beta_{1-40}$ monomer units replicated along the principal axis in order to obtain a continuous structure 6.5 nm long. The best poses obtained from the docking analysis of each compound on each binding site were then used as starting configuration for MD simulation runs, and the molecular mechanics-Poisson-Boltzmann surface area (MM-PBSA) method [44] has been used to obtain an accurate analysis of the stability of the ligand-Aβ protofibril complexes.

The docking poses obtained for the ligands can be clustered into four binding sites, labelled as **β-1 side**, **β-2 side**, **in** and **top**, as shown in **Figure 5**. Moreover, **Table 2** lists the MM-PBSA interaction energy and the probability of the occupancy of each protofibril site, obtained by the docking exercises. In agreement with the previous studies [28,29], the major component of the total free binding energies is given by the van der Waals (vdW) interactions.

The **β-1** binding site comprises the amino acid residues 16-22. The interaction of **C21** with this region was first hypothesized on the basis of the results obtained by solid-state NMR, using dipolar assisted rotational resonance [45]. Successively this site was investigated by computational studies on models of Aβ hexapeptide ^{16}KLVFFA^{21} and full length Aβ fibril [25,27]. The results obtained in the present study indicate a negligible probability for interaction of the ligands with the **β-1** site locate at the external surface of the protofibril. Moreover, only moderate free binding energy was obtained for the ligands at this site (**Table 2**).

However, the ^{16}KLVFFA^{21} stretch of amino acid can also be approached by the ligands after interaction with the **in** binding site (**Figure 5**), which is located inside the upper patch of the β-hairpins (19-34 amino acid residues), and in the **top** binding site, an extended region that involves amino acid residues 15-40, depending on the ligand (**Figure 5**). The **in** binding site was also found in the computational studies by Ngo *et al.* [28,29], and Battisti *et al.*[27]; whereas the **top** binding site has been previously investigated by Kundaikar *et al.* [26] by means of site map analysis.

Finally, the **β-2** binding site is located in the 31-40 region, which is known to modulate fibril aggregation by means of methionine at the position 35 (M35) [46]. Therefore, this binding site is of potential interest to prevent aggregation in this zone [20], and it has been very recently targeted by Battisti *et al.* [27] in their combined computational and experimental study to design curcumin derivatives able to modify the aggregation pattern of Aβ peptides.

Interestingly, all the ligands show a high probability of docking the **top site,** where they realizes loose interaction due to the high mobility during dynamics, whereas better interactions are observed at the **β-2** site (**Table 2**). The **β-1** and **in** binding sites give only a limited contribution to the overall landscape.

Perturbation in the fluctuations due to $A\beta_{1-40}$ fibrils binding can be quantified by the Root Mean Square Fluctuation (RMSF), and values of the fibril-Cα atoms in the absence and presence of the ligands are reported in **Table 2**. In the unbound fibril, the structured β-sheets regions (corresponding to amino acid residues 13-22 and 31-40) show low flexibility with RMSF values of around 0.9 Å, whereas the turn region connecting them (amino acid residues 23-30) shows RMSF values of around 2.5 Å. These observations are in agreement with the recent ssNMR experimental study of Aβ peptide [47] and with the results of structural models of double-layer Aβ segmental polymorphism [48].

Table 2. MM-PBSA binding free energies (kcal mol^{-1}) and probability of ligand occupancy of each binding site (**β-1 side**, **β-2 side**, **in** and **top**). The variation of the RMSF values (Å) of the fibril-Cα atoms (region aa10-40), in the absence and presence of the ligands, are listed for the most significant sites (**β-2 side** and **top)**.

Ligand	P%	$E_{kcal/mol}$	P%	$E_{kcal/mol}$	P%	$E_{kcal/mol}$	P%	$E_{kcal/mol}$	ΔRMF_{top}	$\Delta RMF_{\beta-2}$
	β-1		β-2		in		top		(Å)	(Å)
C21	9	-26,3 ± 4,6	14	-22,4 ± 3,9	5	-28,5 ± 5,2	62	-16,7 ± 3,2	1.5	0.02
K2F21	9	-28,3 ± 5,4	19	-39,7 ± 4,7	5	-46,4 ± 5,3	77	-21,2 ± 9,5	0.5	0.11
PC24	7	-25,8 ± 5,1	30	-36,9 ± 3,8	2	-45,3 ± 4,3	71	-31,4 ± 4,5	1.0	0.03

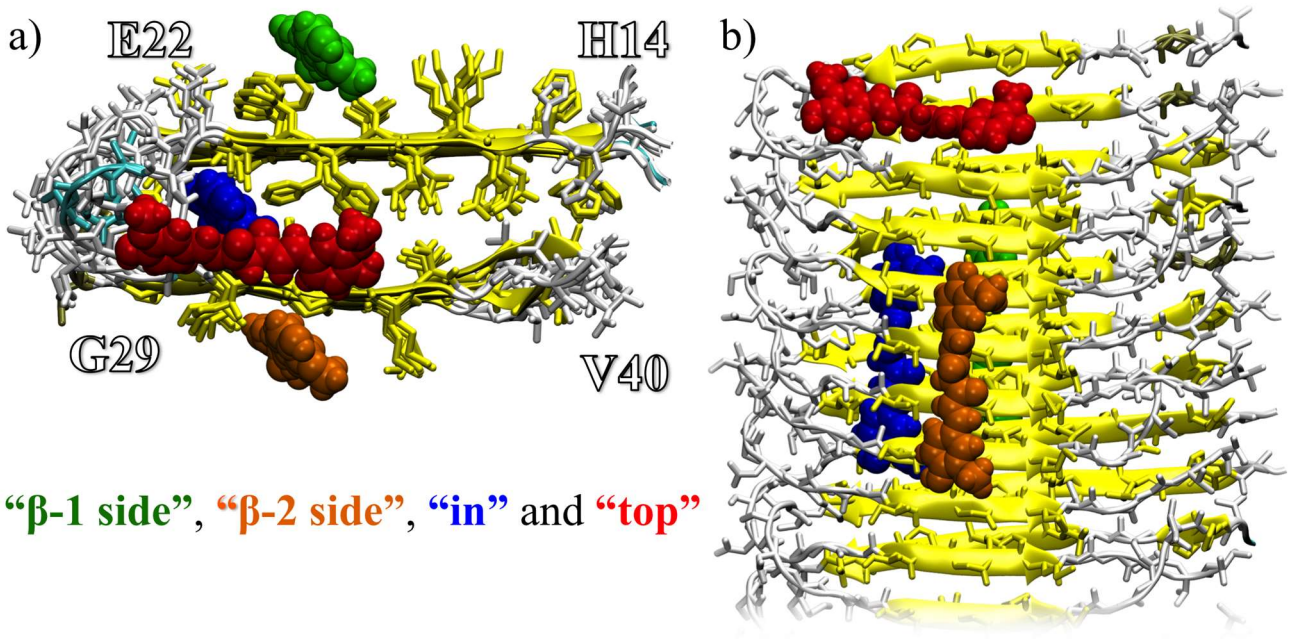

Figure 5. The four main binding sites for the curcuminoid ligands as detected from AutoDock[8]; a) top view, and b) side view. The fibril regions involved in the interactions are labelled as **β-1 side, β-2 side, in** and **top**. The fibril is coloured accordingly to its secondary structure and the ligands with different colours for each docking region.

The analysis of the evolution of the trajectories of the ligand-fibril complexes as a function of time revels that in the **top** pose ligands are rather mobile and travel on the surface of the fibril contacting several residues (**Figure 4 SI**). As a result, curcumin leads to large fluctuations in the natural "dynamic breath" with respect to the isolated fiber; this effect is observed, to a minor extent, also for **K2F21** and **PC24**. On the contrary, the effect at **β-2** site is smaller, stiffening the protofibril.

Previous computational studies also found an increase of flexibility upon curcumin binding to the Aβ peptide [25,26,49]. In particular, Rao *et al*. [25] hypothesized that by increasing the fibril flexibility and promoting conformational changes, curcumin favours the formation of non-neurotoxic intermediate Aβ aggregates including dimers, oligomers, protofibrils, and fibrils in the Aβ-aggregation pathway.

In summary, we can conclude that curcumin shows a significant tendency to destabilize the protofibril by binding to the **top** site. The effect of distortion of the peripheral chain by curcumin may inhibit the process of elongation of the fibril along the principal axes, and/or catalyse the disruption of the β secondary structure. This perturbation is particularly strong at the peptide C-terminals, where M35 lies and can exert an indirect detrimental effect on the conformation/dynamics of this zone responsible for the hierarchical assembly of amyloid fibrils, as also pointed out by Kundaikar *et al.* [26]. Besides the interaction with the **top** site, **K2F21** and **PC24** show also a preference to bind at **β–2** site with moderate perturbative effect on the protofibril dynamics.

Therefore, in order to explain the perturbation induced by ligand binding and the consequent destruction of amyloid aggregates a concurrence of several effects should be invoked. These can be summarized as: a) alteration of the protofibril natural "dynamic breath" upon binding, and b) hiding of the amyloidogenic region by direct binding to the saddle near M35 (**β–2**) or indirectly affecting the M35 conformation and dynamics by binding to other sites.

2.4 Biological activity of curcuminoids on neuronal cells in vitro.

The glutamatergic system plays a key role in synaptic dysfunction and neuronal death induced by Aβ peptide in AD. Excessive extracellular glutamate concentration, due to disrupted glutamate uptake/recycling mechanisms and impaired glutamate neurotransmission, can induce excitotoxicity, a pathological process leading to neuronal cell death [50]. Therefore, we studied whether the curcuminoids with demonstrated disaggregating activity towards Aβ aggregates could exert a protective function in non-receptor mediated oxidative glutamate toxicity in mouse hippocampal HT-22 cells [50]. Through MTT assay, we first evaluated the concentration of glutamate able to halve cell proliferation and we selected 2 mM as IC_{50} dose (**Figure 6 A**). Similarly, we identified the

concentrations at which the selected curcuminoids could have toxic effects on HT-22 cells (**Figure 6 B**).

While curcumin (**C21**) and **K2F21** showed effects on cell viability at 10 μM, **C24** and **PC24** resulted toxic already at 5 μM. We thus selected 1 μM as non toxic dose of curcuminoids that were further investigated for protective effect towards glutamate excitoxicity. Co-administration of curcuminoids to glutamate was able to partially recover cell proliferation and limit glutamate toxicity (**Figure 6 C**). In particular, **C24**, **PC24** and **K2F21** showed similar or higher cytoprotective activity compared to **C21**.

By means of Propidium-Iodide staining, we analyzed the effect of glutamate and curcuminoids co-treatment on cell cycle progression (**Figure 7A**). As expected, glutamate administration increased the number of cells in SubG1 phase, representing apoptotic or necrotic cells, from about 3% in DMSO to 12% in glutamate treated cells (**Figure 7A**). The co-administration with **C21**, **C24**, **PC24** and **K2F21** significantly reduced cell death induced by glutamate. Microscopic analysis of HT-22 cells corroborated the increase in viable cells following co-treatments compared to glutamate alone (**Figure 7 B**).

Since glutamate evokes oxidative stress in HT-22 and consequently activates apoptosis [51], we decided to better characterize the activity of **C24**, **PC24** and **K2F21** *versus* **C21**, through the analysis of the expression levels of key genes involved in oxidative stress and apoptotic cell death. qRT-PCRs showed an increase in the expression levels of inducible nitric oxide synthase (iNOS) following glutamate administration, corroborating the activation of oxidative stress response (**Figure 7 C**). All the tested molecules reduced iNOS transcript levels, with **C24**, **PC24** and **K2F21** working even better than **C21**. To evaluate the anti-apoptotic activity of curcuminoids, we analyzed the *ratio* between the pro-apoptotic Bax and the anti-apoptotic Bcl-2 genes (**Figure 7 D**). The Bax/Bcl-2 *ratio* was arbitrarily set at 1 in control cells. The *ratio,* strongly increased by glutamate administration, was significantly decreased by all tested curcuminoids, consistently with cell cycle data **(Figure 7 A**).

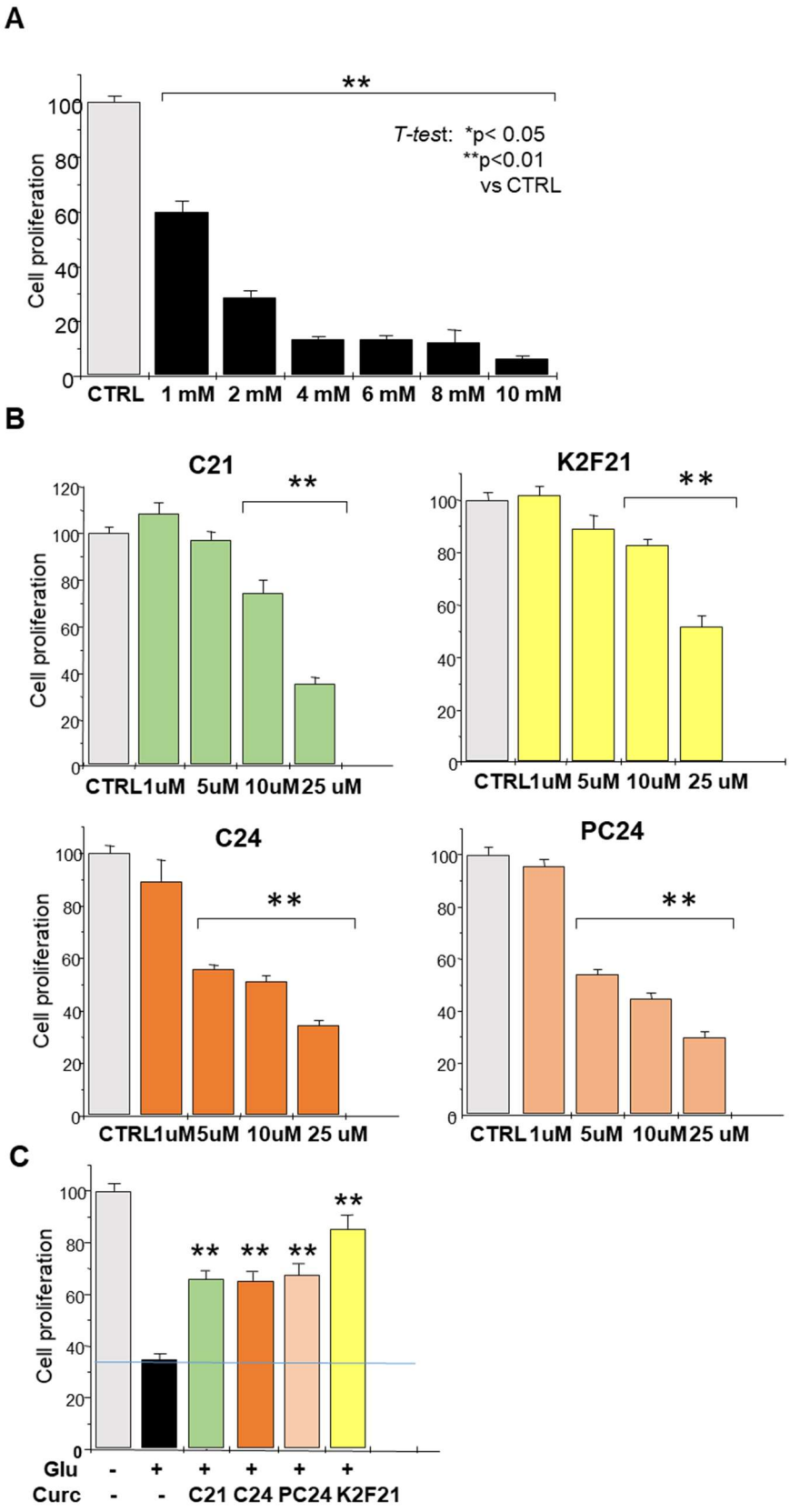

Figure 6. Cytoprotective activity of curcuminoids against glutamate-induced toxicity in hippocampal HT-22 mouse cells. A) Anti-proliferative activity of different concentrations of glutamate compared to control cells (CTRL, its proliferation arbitrarily set at 100%). B) Dose-response effect (1, 5, 10, 25 μM) of the indicated ligands on HT-22 cell proliferation. C) Effect of the co-administration of glutamate (Glu = 2 μM) with curcuminoids (1 μM) on cell proliferation. Data are the mean of at least three independent experiments +/- standard deviation. ** pvalue < 0.01.

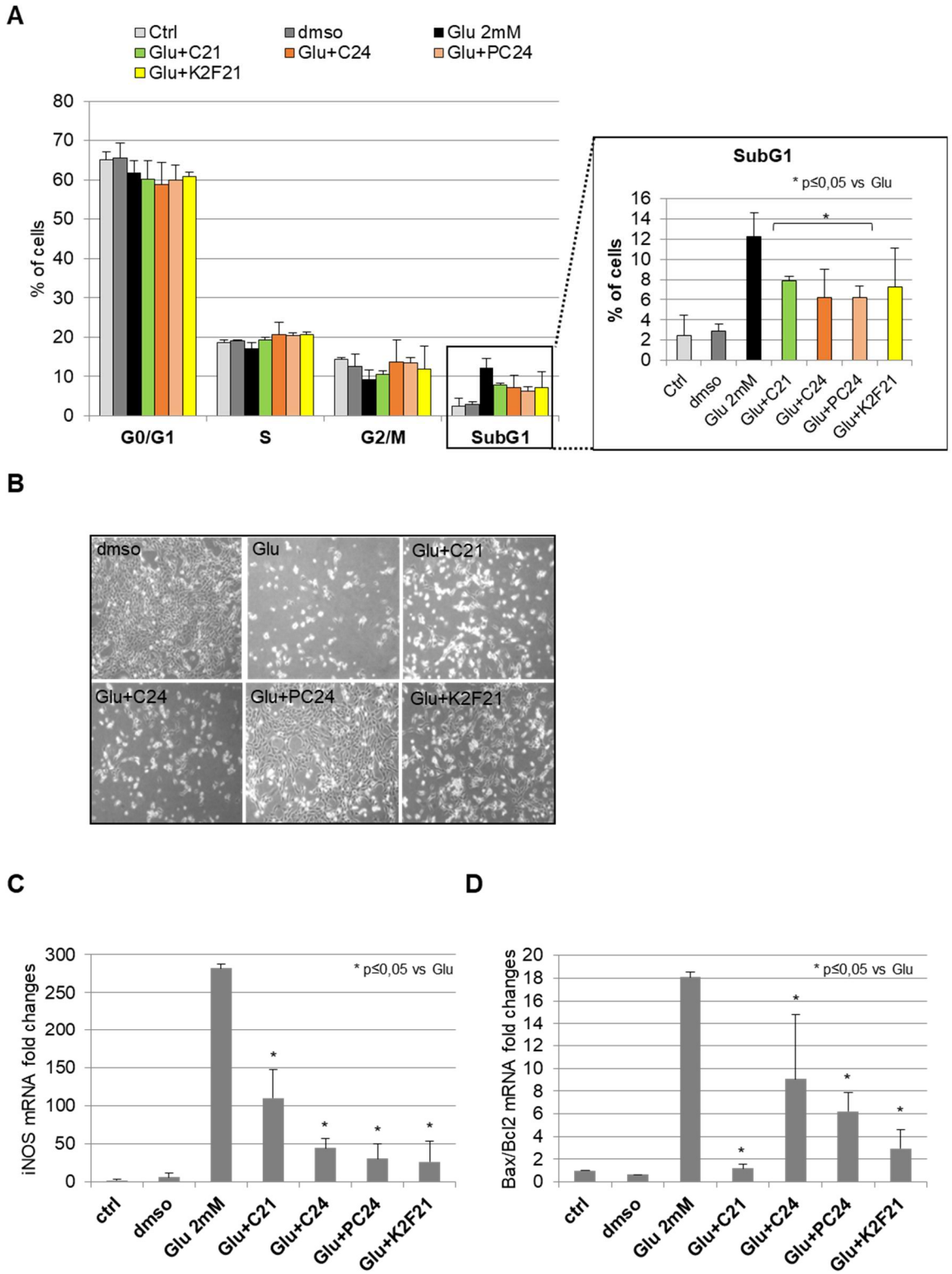

Figure 7. Anti-apoptotic activity of curcuminoids in hippocampal HT-22 mouse cells. **A)** Cytofluorimetric cell cycle analysis of HT-22 cells treated with the indicated molecules (left panel). Right panel: enlargement of the percentages of SubG1 events. Data are the mean of three independent experiments ± SD. **B)** Representative optical microscope images of HT-22 cells treated with DMSO, glutamate or glutamate together with curcuminoids. **C)** qRT-PCR analysis of iNOS transcript in treated or untreated HT-22 cells. Expression levels have been reported as fold change *vs* control cells (ctrl) (arbitrarily set at 1). **D)** Fold changes of the *ratio* between Bax and Bcl2 transcripts, evaluated by qRT-PCR, in control (ctrl), DMSO or glutamate and curcuminoids HT-22 treated cells. The *ratio* in control cells has been arbitrarily set at 1.
* indicates pvalue < 0.05.

3. CONCLUSIONS

On the overall, the presented results suggest that the studied curcumin-based derivatives are able to interfere with Aβ fibrils, and the entity of the exerted effect is modulated by their structure. In particular, the presence of a π-conjugated structure and both peripheral aromatic rings is confirmed to be of utmost importance in Aβ fibrils' interaction, since **B21** and **PB21** showed very weak activity. Moreover, H-donor/acceptor substituents on the aromatic rings are the *sine qua non* structural feature for interaction and disaggregation activity even at very low incubation time. When comparing **C21**, **PC21** and **K2F21**, only minor differences are observed in the interaction with Aβ fibrillar aggregates. Upon binding, the ligands modify the conformational dynamic and/or interact with the amyloidogenic region of the protofibril facilitating disaggregation, as demonstrated by computational simulations. However, since the ligand binding is non-specific, the Aβ fibrils display several partially or not overlapping binding sites, in which dispersion interactions (vdW) act as the driving force.

Significantly, *in vitro* results on hippocampal cells demonstrate that the molecules are safe if administered at low concentrations, and can protect from glutamate toxicity.

To wrap up, this study pinpointed the importance of vanillin aromatic structure of curcuminoids to accomplish both interaction with Aβ fibrils and cytoprotection against oxidative stress, while substitution on β-diketo moiety (K series) or the presence of pyrazole ring (P series) have effect on increasing stability in physiological conditions, and hopefully bioavailability in further *in vitro* and *in vivo* investigations.

On the whole, among all compounds, **K2F21** stands out as the best candidate for both diagnostic/therapeutic purposes, due to its high stability in physiological conditions, its rapid binding to fibrillar aggregates and strong depolymerizing activity, high cytoprotection against oxidative stress and low cytotoxicity.

4. EXPERIMENTAL SECTION

4.1 Chemistry

All chemicals were reagent grade and used without further purification unless otherwise specified. Elemental analyses were performed on ThermoScientific^{TM} FLASH 2000 organic elemental analyzer. UV-visible spectra were recorded with a Jasco V-570 UV/Vis/NIR spectrophotometer at 298 K in the 250–600 nm spectral range employing quartz cells (1 cm optical path).

Liquid chromatography – mass spectrometry (LC-MS) experiments were performed on an Agilent 6300 Ion Trap LC-MS system equipped with an electrospray ionisation (ESI) interface. The compounds were separated using Agilent Zorbax SB C18 30×2.1 mm, 3.5 µm. Samples were prepared in MeOH and diluted to 10 ppm in MilliQ water; blank was MilliQ water. Eluent phase:

pump A H_2O (formic acid 1%), pump B CH_3CN (formic acid 1%), gradient: 10 % of B for 1 minute, 10% –100% of B for 5 minutes, then 100 % of B for 4 minutes, flux 0.3 mL min^{-1}, injection volume 10 µL. The ion spectra were obtained in positive mode, using a scan range between *m/z* 100 and 1500. High-purity nitrogen was used as the nebuliser and the drying gas. The nitrogen drying gas was at a constant flow rate of 10 L min^{-1}, heated to 350 °C. The nebuliser gas pressure was 32 psi and the capillary voltage was 3.5 kV.

NMR spectra were recorded on a Bruker FT-NMR AVANCE III HD 600 MHz spectrometer with 5mm CryoProbe BBO H&F at 298 K. Nominal frequencies were 600.13 MHz for ^{1}H and 150.9 MHz for ^{13}C. For each sample, ~5 mg were weighed and diluted up to 0.6 mL with the proper deuterated solvent into 5 mm NMR tube. 90° pulse was calibrated for each sample and standard NMR parameters were used to achieve quantitative results (relaxation delay 10 s). Proton and carbon chemical shifts are given in parts per million (ppm) *versus* external TMS, and were determined by reference to the solvent residual signals (7.26 for $CHCl_3$ and 2.05 ppm for CD_2HCOCD_3 for proton, and 77.2 for $CDCl_3$ and 29.8 ppm for $(CD_3)_2CO$ for carbon). Typical 2D homo- and hetero-nuclear techniques were used for assignment, i.e. ^{1}H,^{1}H-COSY, ^{1}H,^{13}C-HSQC, ^{1}H,^{13}C-HMBC. ^{1}H and ^{13}C NMR spectra for all compounds are reported in Supplementary Information. The purity of final compounds was determined to be at least 95% pure by a combination of HR-MS, NMR, and elemental analysis.

4.1.1 Synthesis.

Compounds **C23**, **C24**, **C33** and **PC21** were synthesized as reported in the literature [36,52–54].

4-hydroxy-6-(4-hydroxy-3-methoxyphenyl)-(3Z,5E)-3,5-esadien-2-one (**B21**). This compound was synthesized by a modification of a procedure reported in the literature [55]. A suspension of boric anhydride (10 mmol) and 2,4-pentandione (10 mmol) in DMF (12 mL) was stirred for 30 min at 80 °C, then tributylborate (4 mmol) was added, and the mixture was kept under stirring at 80 °C overnight. Vanillin (2 mmol) was added and followed by slow addition of *n*-butylamine (0.4 mmol in 0.5 mL of DMF). After stirring at 80 °C for 6 h, the solution was acidified with HCl 0.5 M (30 mL) under heating at 80 °C, then cooled down to room temperature. The aqueous phase was extracted with ethyl acetate, then the organic phases were washed with $NaHCO_3$ 5% and brine, before anhydrification under $MgSO_4$. The crude product was purified by flash-column chromatography (silica gel, gradient: petroleum ether/ethyl acetate from 90/10 *v/v* to 30/70 *v/v*). Yellow powder, 40% yield. Elemental analysis calc. (%) for $C_{13}H_{14}O_4$ (234.25 g/mol): C, 66.66; H, 6.02. Found: C, 67.05; H, 6.17. LC-MS (ESI): *m/z* 235.1 $[M+H]^+$. ^{1}H NMR ($CDCl_3$): δ *(ppm)* 5.79 (H-1, s, 1H), 6.51 (H-3, d, 1H), 2.15 (H-3', s, 3H), 7.54 (H-4, d, 1H), 7.21 (H-6, d, 1H), 6.83 (H-9, d, 1H), 7.09 (H-10, dd, 1H), 3.92 (OC$\underline{H_3}$, s, 3H). ^{13}C NMR ($CDCl_3$): δ *(ppm)* 100.0 (C-1), 178.1 (C-2), 197.4 (C-2'), 119.2

(C-3), 25.3 (C-3'), 140.3 (C-4), 127.2 (C-5), 110.4 (C-6), 148.1 (C-7), 149.1 (C-8), 115.2 (C-9), 122.7 (C-10), 55.2 (O<u>C</u>H$_3$). Atom numbering refers to **Scheme 1 SI**.

3,5-bis[(E)-2-(3-methoxyphenyl)ethenyl]-1H-pyrazole (**PB21**). This compound was synthesized by a modification of a procedure reported in the literature [56]. **B21** (2 mmol) was dissolved in glacial acetic acid (20 mL) and kept under stirring at 70 °C for 30 min, then hydrazine monohydrate (8 mmol) was added dropwise. The reaction was stopped after 8 h by removal of solvent under reduced pressure. The crude product was suspended in water, filtered and purified by flash-column chromatography (ethyl acetate/*n*-hexane 9/1 *v/v*). Pale yellow powder, 80% yield. Elemental analysis calc. (%) for $C_{13}H_{14}N_2O_2$ (230.26 g/mol): C, 67.81; H, 6.13; N, 12.17. Found: C, 67.75; H, 6.18; N, 12.10. LC-MS (ESI): *m/z* 231.3 $[M+H]^+$. ^{1}H NMR ($(CD_3)_2CO$): *δ (ppm)* 9.06 (NH, s, 1H), 6.24 (H-1, s, 1H), 6.96 (H-3, d, 2H), 2.27 (H-3', s, 3H), 7.03 (H-4, d, 2H), 7.19 (H-6, d, 2H), 6.82 (H-9, d, 2H), 6.98 (H-10, dd, 2H), 3.91 (OC<u>*H*$_3$</u>, s, 6H). ^{13}C NMR ($(CD_3)_2CO$): *δ (ppm)* 101.2 (C-1), 147.8 (C-2), 143.2 (C-2'), 117.1 (C-3), 10.0 (C-3'), 129.1 (C-4), 129.5 (C-5), 108.9 (C-6), 147.8 (C-7), 146.7 (C-8), 115.1 (C-9), 120.2 (C-10), 55.4 (O<u>C</u>H$_3$). Atom numbering refers to **Scheme 1 SI**.

4,4'-[1H-pyrazole-3,5-diyldi(E)ethene-2,1-diyl]bis(2-methoxyphenol)] (**PC21**). Synthesis of PC21 was performed as previously reported [56]. Orange powder, 80% yield. Elemental analysis calc. (%) for $C_{21}H_{20}N_2O_4$ (364.39 g/mol) C 69.22%, H 5.53%, N 7.69%. Found: C 69.13%, H 5.62 %, N 7.75 %. LC-MS-IT m/z 365.4 $(M + H)^+$. ^{1}H NMR ($(CD_3)_2CO$): *δ (ppm)* 9.17 (NH, s, 1H), 6.68 (H-1, s, 1H), 7.02 (H-3, d, 2H), 7.14 (H-4, d, 2H), 7.22 (H-6, d, 2H), 6.85 (H-9, dd, 2H), 7.01 (H-10, dd, 2H), 3.92 (OC<u>H$_3$</u>, s, 6H). ^{13}C NMR ($(CD_3)_2CO$): *δ (ppm)* 98.94 (C-1), 146.94 (C-2), 120.83 (C-3), 129.85 (C-4), 129.45 (C-5), 108.89 (C-6), 147.75 (C-7), 146.94 (C-8), 115.19 (C-9), 120.4 (C-10), 54.77 (O<u>C</u>H$_3$). Atom numbering refers to **Scheme 1 SI**.

1H-pyrazole-3,5-diylbis[(E)ethene-2,1-diyl(2-methoxyphenyl-4,1-diyl] diacetate (**PC24**). This compound was obtained by direct acetylation of **PC21** [52]. Light brown powder, 20% yield. Elemental analysis calc. (%) for $C_{25}H_{24}N_2O_6$ (448.47 g/mol): C, 66.95; H, 5.39; N, 6.2. Found: C, 66.83; H, 5.42; N, 6.18. LC-MS (ESI): *m/z* 449.4 $[M+H]^+$. ^{1}H NMR ($(CD_3)_2CO$): *δ (ppm)* 5.64 (H-1, s, 1H), 7.27 (H-3, d, 2H), 7.78 (H-4, d, 2H), 7.34 (H-6, d, 2H), 6.89 (H-9, d, 2H), 7.08 (H-10, dd, 2H), 3.97 (OC<u>*H*$_3$</u>, s, 6H), 2.70 (OCOC<u>*H*$_3$</u>). ^{13}C NMR ($(CD_3)_2CO$): *δ (ppm)* 55.4 (C-1), 146.5 (C-2), 134.0 (C-3), 114.8 (C-4), 129.5 (C-5), 109.1 (C-6), 147.8 (C-7), 146.9 (C-8), 115.2 (C-9), 120.9 (C-10), 55.4 (O<u>C</u>H$_3$), 22.2 (OCO<u>C</u>H$_3$), 170.7 (O<u>C</u>OCH$_3$). Atom numbering refers to **Scheme 1 SI**.

3,5-bis[(E)-2-phenylethenyl]-1H-pyrazole (**PC33**). Synthesis of **PC33** was performed as previously reported, starting from **C33** [56]. Light yellow powder, 80% yield. Elemental analysis calc. (%) for $C_{19}H_{16}N_2$ (272.34 g/mol): C, 83.79; H, 5.92; N, 10.29. Found: C, 83.72; H, 5.98; N, 10.02. LC-MS (ESI): *m/z* 273.3 $[M+H]^+$. ^{1}H NMR ($(CD_3)_2CO$): *δ (ppm)* 9.06 (NH, s, 1H), 6.82 (H-1, s, 1H), 7.20

(H-3, d, 2H), 7.25 (H-4, d, 2H), 7.58 (H-6/H-10, d, 4H), 6.39 (H-7/H-9, d, 2H), 7.29 (H-8, d, 2H). ^{13}C NMR ($(CD_3)_2CO$): *δ (ppm) 100*.0 (C-1), 146.5 (C-2), 118.5 (C-3), 129.7 (C-4), 137.2 (C-5), 126.3 (C-6/C-10), 128.8 (C-7/C-9), 127.7 (C-8). Atom numbering refers to **Scheme 1 SI**.

2-(4-acetyl-5-oxohexyl)-1H-isoindole-1,3(2H)-dione (**K3F**). 2,4-pentandione (25 mmol) is added to a suspension of K_2CO_3/KI (50/3 mmol) in dry acetone (15 ml) at 80 °C and kept under stirring for 1 h. Then, a solution of 2-(3-bromopropyl)-1*H*-isoindole-1,3(2*H*)-dione (25 mmol) in dry acetone (5 mL) is added dropwise. After stirring overnight at 80°C, the solution was diluted with aqueous NH_4Cl and extracted twice with CH_2Cl_2. The organic phase was washed with brine and dried over Na_2SO_4. Removal of the solvent afforded an oily residue, which was purified through distillation under reduced pressure to give the desired product as yellow oil (yield 45%). Elemental analysis calc. (%) for $C_{16}H_{17}NO_4$ (287.31 g/mol): C, 66.89; H, 5.96; N, 4.88. Found: C, 67.00; H, 6.01; N, 4.95. LC-MS (ESI): *m/z* 288.3 $[M+H]^+$. ^{1}H NMR (CD_3OD): *δ (ppm)* 2.15 (H-3/H-3', s, 6H), 2.32 (H-11, t, 2H) 1.83 (H-12, m, 2H), 3.77 (H-13, t, 2H), 7.88 (H-16, dd, 2H), 7.77 (H-17, dd, 2H); ^{13}C NMR (CD_3OD): *δ (ppm)* 109.1 (C-1), 190.0 (C-2), 26.0 (C-3), 25.1 (C-11), 29.1 (C-12), 37.8 (C-13), 168.5 (C-14), 123.3 (C-15), 132.5 (C-16), 134.0 (C-17). Atom numbering refers to **Scheme 2 SI**.

2-(3-acetyl-4-oxopentyl)-1H-isoindole-1,3(2H)-dione (**K2F**). This compound was obtained as **K3F** using 2-(2-bromoethyl)-1H-isoindole-1,3(2H)-dione. Yellow oil, 40% yield. Elemental analysis calc. (%) for $C_{15}H_{15}NO_4$ (273.28 g/mol): C, 65.92; H, 5.53; N, 5.13. Found: C, 65.88; H, 5.59; N, 5.10. LC-MS (ESI): *m/z* 274.3 $[M+H]^+$. ^{1}H NMR ($CDCl_3$): *δ (ppm)* 2.63 (H-3/H-3', s, 6H), 3.56 (H-11, t, 2H), 4.04 (H-12, t, 2H), 7.80 (H-16, m, 2H), 7.69 (H-17, m, 2H); ^{13}C NMR ($CDCl_3$): *δ (ppm)* 108.1 (C-1), 189.0 (C-2), 36.8 (C-3), 28.3 (C-11), 39.1 (C-12), 167.7 (C-14), 131.9 (C-15), 123.4 (C-16), 134.1 (C-17). Atom numbering refers to **Scheme 2 SI**.

(2-((4Z,6E)-5-hydroxy-7-(4-hydroxy-3-methoxyphenyl)-4-((E)-3-(4-hydroxy-3-ethoxyphenyl)acryloyl) hepta-4,6-dien-1-yl)isoindoline-1,3-dione (**K3F21**). This compound was synthesized as other similar curcuminoids, using K3F and vanillin as reagents [34] . The crude product was recrystallized from EtOH to give the title compound as red powder (yield: 15%). Elemental analysis calc. (%) for $C_{32}H_{29}NO_8$ (555.58 g/mol): C, 69.18; H, 5.26; N, 2.52. Found: C, 68.97; H, 5.32; N, 2.60. LC-MS (ESI): *m/z* 556.3 $[M+H]^+$. ^{1}H NMR ($CDCl_3$): *δ (ppm)* 6.72 (H-3, d, 2H), 7.63 (H-4, d, 2H), 7.06 (H-6, d, 2H), 6.94 (H-9, d, 2H), 7.12 (H-10, dd, 2H), 1.93 (H-11, t, 2H), 1.49 (H-12, m, 2H), 3.70 (H-13, t broad, 2H), 7.85 (H-16, m, 2H), 7.73 (H-17, m, 2H). ^{13}C NMR ($CDCl_3$): *δ (ppm)* 109.0 (C-1), 182.8 (C-2), 121.3 (C-3), 145.1 (C-4), 128.3 (C-5), 109.6 (C-6), 147.2 (C-7), 148.3 (C-8), 114.8 (C-9), 124.3 (C-10), 27.8 (C-11), 23.2 (C-12), 38.0 (C-13), 168.0 (C-14), 132.3 (C-15), 123.1 (C-16), 133.9 (C-17). Atom numbering refers to **Scheme 2 SI**.

2-((4Z,6E)-4-cinnamoyl-5-hydroxy-7-phenylhepta-4,6-dien-1-yl)isoindoline-1,3-dione (**K3F33**). This compound was obtained as **K3F21** from **K3F** and benzaldehyde, yielding a yellow powder (yield: 35%). Elemental analysis calc. (%) for $C_{30}H_{25}NO_4$ (463.52 g/mol): C, 77.74; H, 5.44; N, 3.02. Found: C, 77.63; H, 5.52; N, 3.09. LC-MS (ESI): *m/z* 464.2 $[M+H]^+$. ^{1}H NMR ($CDCl_3$): *δ (ppm)* 7.07 (H-3, d, 2H), 7.80 (H-4, d, 2H), 7.60 (H-6/H-10, m, 4H), 7.42 (H-7/H-8/H-9, m, 6H), 2.67 (H-11, t, 2H), 2.04 (H-12, m, 2H), 3.91 (H-13, t broad, 2H), 7.92 (H-16, m, 2H), 7.79 (H-17, m, 2H). ^{13}C NMR ($CDCl_3$): *δ (ppm)* 110.4 (C-1), 182.7 (C-2), 120.1 (C-3), 142.1 (C-4), 135.2 (C-5), 128.5 (C-6/C-10), 129.0 (C-7/C-9), 130.1 (C-8), 23.7 (C-11), 30.8 (C-12), 37.7 (C-13), 168.5 (C-14), 134.3 (C-15), 123.3 (C-16), 134.1 (C-17). Atom numbering refers to **Scheme 2 SI**.

2-((3Z,5E)-4-hydroxy-6-(4-hydroxy-3-methoxyphenyl)-3-((E)-3-(4-hydroxy-3-methoxyphenyl) acryloyl) hexa-3,5-dien-1-yl) isoindoline-1,3-dione (**K2F21**). This compound was obtained as **K3F21** from **K2F** and vanillin, yielding a red powder (yield: 20%). Elemental analysis calc. (%) for $C_{31}H_{27}NO_8$ (541.55 g/mol): C, 68.75; H, 5.03; N, 2.59. Found: C, 68.63; H, 5.12; N, 2.55. LC-MS (ESI): *m/z* 542.2 $[M+H]^+$. ^{1}H NMR ($CDCl_3$): *δ (ppm)* 7.29 (H-3, d, 2H), 7.75 (H-4, d, 2H), 7.47 (H-6, dd, 2H), 6.99 (H-9, dd, 2H), 7.20 (H-10, dd, 2H), 2.90 (H-11, t, 2H), 3.89 (H-12, t (broad), 2H), 2H), 7.88 (H-16, m, 2H), 7.83 (H-17, m, 2H), 4.15 (OC$\underline{H_3}$). ^{13}C NMR ($CDCl_3$): *δ (ppm)* 106.7 (C-1), 183.1 (C-2), 117.6 (C-3), 142.4 (C-4), 128.1 (C-5), 109.1 (C-6), 147.1 (C-7), 148.1 (C-8), 114.6 (C-9), 124.1 (C-10), 25.7 (C-11), 38.6 (C-12), 168.0 (C-14), 132.2 (C-15), 133.9 (C-16), 123.0 (C-17), 56.2 (O$\underline{C}H_3$). Atom numbering refers to **Scheme 2 SI**.

4.1.2 Kinetics stability at physiological conditions. The chemical stability of the selected curcuminoids **C23**, **C24**, **PC21**, **PC24** and **K2F21** at 37 °C in darkness was evaluated by UV−vis spectroscopy. The change in absorbance in the 250−600 nm range over an overall period of 24 h was recorded for 50 μM solutions of the compounds in phosphate buffered solution (PBS) 0.01 M at pH 7.4. A constant ionic strength of 0.1 M (NaCl) was maintained in all experiments.

4.1.3 Spectrophotometric pH-dependent titrations. 50 μM aqueous solution of selected compounds (**B21**, **K3F21** and **PC21),** obtained by dilution of 2.50×10^{-3} M methanol solution, was investigated in the 250−600 nm range on varying pH by negligible additions of concentrated NaOH or HCl (4 M) in the 2–11 (**PC21**) or 5-11 (**B21**, **K3F21)** pH range. The overall protonation constants ($\log\beta_{qr}$) were evaluated from spectrophotometric data using computer program HypSpec [40].

4.2 Studies on $A\beta_{1\text{-}40}$ peptide *in vitro*.

Recombinant human $A\beta_{1\text{-}40}$ peptide (Cat #A-1001) was purchased from rPeptide Company (Georgia, USA). $A\beta_{1\text{-}40}$ was dissolved in aqueous NaOH 10 mM to reach 665 μM stock concentration defined by UV-Vis spectroscopy using extinction coefficient 2300 M^{-1} cm^{-1} at λ = 292 nm. The solution was

sonicated for 1 min in bath sonicator, and centrifuged for 10 min at 4 °C and 12000 rpm. The concentration of solution was checked spectrophotometrically. For amyloid fibril preparation, the stock solution was incubated for 5 days at 37 °C without agitation.

The stock solution of $A\beta_{1-40}$ amyloid fibrils was diluted with 150 mM 3-(N-morpholino) propanesulfonic acid (MOPS) buffer (0.035% NaN_3, pH = 6.9) to a final concentration of 10 μM. Curcuminoid derivative at 10 μM concentration was added to solution of 10 μM amyloid fibrils and incubated for 24 h at 37 °C. The interference of derivatives with $A\beta_{1-40}$ fibrils was evaluated using Thioflavin T (ThT) fluorescence assay and atomic force microscopy. For quantification of the destroying ability the interference of the studied curcumin derivatives were examined for samples containing 10 μM $A\beta_{1-40}$ fibrils and derivative in the concentration range 100 pM – 1 mM, using ThT assay. Briefly, ThT was added to the samples containing 10 μM $A\beta_{1-40}$ fibrils alone and after treatment with curcuminoid to 20 μM final concentration. The samples were incubated at 37 °C for 1 h in the dark. Then, the samples were excited at 440 nm (slit width 9 nm) and the subsequent emission was measured between 465 and 600 nm (slit width 9 nm) with maximal fluorescence intensity peak at 485 nm. ThT fluorescence intensities were detected in black 96-well plates using a Synergy Mx (BioTek Company, USA) well plate reader. To measure the intrinsic fluorescence of the tested compounds the peptide was replaced with buffer solution. The volume of DMSO in measuring samples was lower than 2% and has no effect on the stability of $A\beta_{1-40}$. All ThT experiments were performed in triplicate and the final value is the average of measured values with standard deviation (± SD).

Samples for Atomic Force Microscopy (AFM) were prepared by spreading solutions of 10 μM fibrils and 10 μM derivatives on a freshly cleaved mica surface and leaving them for 5 min to adsorb on the surface. After 5 min adsorption, the samples were washed with ultrapure water (18.2 MΩ cm) and left to dry under nitrogen. AFM images were taken using a Scanning Probe Microscope (Veeco di Innova, Bruker AXS Inc., Madison, USA) in a tapping mode using an NCHV cantilever with specific resistance of 0.01 – 0.025 Ω cm, antimony (n) doped Si, radius of the tip curvature of 10 nm. The resolution of image was 512 pixels per line (512 × 512 pixels per image) and scan rate 0.5 kHz. No smoothing or noise reduction was applied.

Interaction of curcumin derivatives with $A\beta_{1-40}$ fibrils leading to their destroying was characterized using DC_{50} values (half-maximal concentration with 50% destroying activity). The destruction of $A\beta_{1-40}$ (concentration was fixed at 10 μM) induced by increasing concentration of curcuminoid derivatives ranging from 100 pM to 1 mM was detected using ThT assay. ThT fluorescence intensities measured in the presence of derivatives were normalized to the fluorescence signal of amyloid fibrils alone. The final DC_{50} value represents the average value obtained by fitting three independent concentration dependencies with the non-linear least-squares method (SigmaPlot:

sigmoidal, 3-parameters logistic: $y = a / [1 + \exp(x - x_0)/b]$ where x_0 corresponds to DC_{50} value). To measure the intrinsic fluorescence of the tested compounds the peptide was replaced with buffer solution. The volume of DMSO in measuring samples was lower than 2% and has no effect on the stability of fibrils and $A\beta_{1-40}$ fibrillization.

4.3 Computational details.

The structure of **C21**, **K2F21** and **PC24** each curcumin derivative was built in its DK form, except for **C21**, for which both the DK and KE forms were considered. The simulation results are essentially the same, therefore we reported the results for the KE form. The force field for each derivative was built in the Gromacs format [57] by using the Automated Topology Builder[58,59] (ATB) web server.

The structural model of Aβ fibrils formed by the 40-residue peptide based on numerous constraints from solid state NMR and electron microscopy was retrieved from the Protein Data Bank (PDB ID: 2LMN [60]). The missing N-terminal peptide region of Aβ peptide was built using the Molefacture plugin in the VMD package [61] as random coils as predicted by both the Jpred web server [62] and by the Modeller package [63] for protein secondary structure assignments.

4.3.1 Molecular Docking

The binding modalities of the compounds studied with the $A\beta_{1-40}$ fibril were investigated by means of the AutoDock [64] program. The Aβ fibril was built by replicating the monomeric unit 10 times along its principal axis obtaining a continuous structure 6.5 nm long. The region of the fibril used to perform the docking comprises the β, β2 β-sheets and the coil connecting them (amino acid residues from 13 to 40). The N-terminal region was not considered because of its high mobility. The fibril was kept rigid, whereas flexibility was allowed to the compounds in order to obtain a good accuracy and affordable computational costs.

A grid of 126 × 126 × 126 points, with a grid spacing of 0.375 Å, was selected. It was centred at centre of mass of the first five monomers, with the aim of covering half of the whole the fibril surface. The docking of the ligands was performed using the Lamarckian Genetic Algorithm with a population of 150 individuals, during 200 runs for 27000 generations with 25 million energy evaluations. The docking results were afterward clustered setting an RMS tolerance value of 2.0, to identify the principal orientations of the ligands. The most representative structure of each of the principal clusters for every ligand/docking system was selected for further analysis.

4.3.2 Molecular Dynamics Simulations.

Molecular dynamics simulations were performed with GROMOS 54a7 force field [65]. This force fields has been shown to improve the stability of secondary structure elements, while retaining

the agreement with observed data such as NOE intensities and 3J-couplings [65]. Very recently, the a99SB-disp, a force field of the Amber family, has been developped to achieve excellent agreement with experiment for disordered proteins, while maintaining state-of-the-art accuracy for folded proteins [66]. However, a recent work on the interaction of natural compounds on full-length $A\beta_{40}$ fibrils showed that the Gromos54a7 force field is able to grasp the destabilizing effects on the rotein structure upon binding [67].

Simple point charge (SPC) water [68] was added to the simulation box (7.5 × 9.7 × 8.0 nm) and a salt concentration of 150 mM NaCl was used to neutralize the system. The particle-mesh Ewald (PME) algorithm was used to calculate long-range electrostatics [69,70] with a fourth-order cubic interpolation, a grid spacing of 0.16 nm, and a real-space cutoff of 1 nm. Both van der Waals and neighbour list cutoffs describing short-range interactions were set to 1.0 nm. The temperature in all simulations was kept constant at 310 K and the pressure was set to 1 bar in order to mimic physiological conditions. The temperature was controlled using a velocity-rescaling thermostat with a coupling time of 0.1 ps. During the equilibration run the pressure was controlled by the Berendsen barostat, while during the production run by the Parrinello-Rhaman barostat with coupling time of 2 ps and an isothermal compressibility of 4.5×10^{-5} bar^{-1}. All computational simulations (production runs) were 100ns long and the time step used was 2.0 fs. Data analysis were performed using the Gromcas-5.0.4 package[71].

MM_PBSA [44,72] is based on the single-trajectory approach, thus 250 snapshots (25 ns) sampled over the course of the 100 ns simulation were used, starting the calculation when the system reached an equilibrium configuration (approximately after 10 ns of the beginning of the production run).

4.4 Cell culture and treatments.

The mouse clonal hippocampal neuronal cell line HT-22 was a generous gift from Dr. Pamela Maher (The Salk Institute for Biological Studies, La Jolla, San Diego, CA). Cells were maintained at 37 °C and 5% CO_2 in high-glucose Dulbecco's Modified Eagle Medium (DMEM) supplemented with 10% heat-inactivated (56 °C, 30 min) fetal bovine serum (FBS-Gibco), 50 U/mL penicillin, 50 mg/mL streptomycin, 5 mM glutamine (Biowest). Cells were harvested and cultured in 96- or 6-well plates according to the requirement of the experiment.

To examine the effect of **C21**, **C24**, **PC24** and **K2F21**, cells were treated the day after plating with different concentrations (1, 2, 5, 10, 25 μM in complete medium) for 24 h. A stock solution of the drugs (10 mM) was prepared in DMSO and diluted in culture medium keeping the final DMSO concentration at 0.025%. The same concentration of DMSO was used as negative control. To examine

the effect of glutamate (#G8415-Sigma Aldrich) cells were exposed to different concentrations (1, 2, 4, 6, 8, 10 mM) in complete medium for 24 h. **C21**, **C24**, **PC24** and **K2F21** (1 μM) were added to the media containing glutamate 2 mM for the co-treatment. The selection of concentrations was based on the results of MTT assays.

4.4.1 Cell viability assay (MTT assay)

Cell viability was determined through the analysis of the conversion of MTT to MTT-formazan by mitochondrial enzymes as follows. HT-22 cells (5×10^3) plated in 96-well plates were treated for 24 h with **C21**, **C24**, **PC24**, **K2F21** and glutamate, or co-treated with curcuminoids and glutamate at the selected concentrations. After 24 h at 37 °C, 150 μL of MTT solution (5 mg/mL Thiazolyl Blue Tetrazolium Bromide in PBS) was added to cells at a final concentration of 0.5 mg/ml per well and incubated for 2 h at 37 °C. The medium was then removed carefully and 150 μL of MTT solvent (4 mM HCl, 0.1% NP40 in isopropyl alcohol) was added to resolve the blue formazan in living cells. After 15 min of incubation with a gently shaking in the dark, the absorbance at 570 nm was read with an ELISA reader (Multiskan FC, ThermoScientific).

4.4.2 Flow cytometric cell cycle analysis

HT-22 cells (1.5×10^5) plated in 6-well plates were co-treated with glutamate and curcuminoids at the selected concentrations, for 24 hours. Cell pellets were then collected by centrifugation, washed with PBS and resuspended in 400 μl of PI solution (0.1%, Triton, 3.4 M Na citrate, 50 μg/mL Propidium Iodide). After 30 min of incubation, cells were analyzed for DNA content using cytofluorimeter (Beckman coulter).

4.4.3 mRNA expression analysis (RT-PCR)

RNA was extracted from cells by using RNeasy mini kit (Qiagen, Hilden, Germany), according to the manufacturer's protocol. For cDNA synthesis, 1 μg of RNA was retrotranscribed with a Moloney murine leukemia virus reverse transcriptase (RT) (Promega). Quantitative Real-Time PCR was performed with SsoAdvanced Universal SYBR Green Supermix (Biorad) in a Roche LC480 Cycler. mRNA amplification was performed with the following oligonucleotides: Rplp0 forward: 5'-GAGCCAGCGAGGCCACACTG -3'; Rplp0 reverse: 5'- CCACGTTGCGGACACCCTCC -3'; Bax forward: 5'- AGGGTTTCATCCAGGATCGAGCAG -3'; Bax reverse: 5'-ATCTTCTTCCAGATGGTGAGCGAG -3'; Bcl2 forward: 5'- CACAGAGGGGCTACGAGTG-3'; Bcl-2 reverse: 5'- CAAAGGCATCCCAGCCTCC-3'; iNOS forward: 5'-ACGAGACGGATAGGCAGAGA- 3'; iNOS reverse: 5'- GAGTAGTAGCGGGGCTTCAA-3'.

Expression levels of target genes were normalized to the levels of the housekeeping gene Rplp0. The relative fold change expression of sample was calculated with the comparative ΔΔCt method [73].

ACKNOWLEDGMENTS

This work was supported by the University of Modena and Reggio Emilia through the project "Rational design of curcumin-based bifunctional ligands for early diagnosis and therapy of Alzheimer's disease (FONDO DI ATENEO PER LA RICERCA ANNO 2015)". ZG and ZB were supported by the research grant projects in frame of VEGA 2/0145/17, 2/0030/18, MVTS COST 083/14 action BM1405 and SAS-MOST JRP 2015/5.

References

[1] W.R. Bevan-Jones, A. Surendranathan, L. Passamonti, P. Vázquez Rodríguez, R. Arnold, E. Mak, L. Su, J.P. Coles, T.D. Fryer, Y.T. Hong, G. Williams, F. Aigbirhio, J.B. Rowe, J.T. O'Brien, Neuroimaging of In fl ammation in Memory and Related Other Disorders (NIMROD) study protocol: a deep phenotyping cohort study of the role of brain in fl ammation in dementia, depression and other neurological illnesses, BMJ Open. 7 (2017) e013187. http://bmjopen.bmj.com/content/bmjopen/7/1/e013187.full.pdf (accessed July 26, 2017).

[2] Y.C. Wong, D. Krainc, α-synuclein toxicity in neurodegeneration: mechanism and therapeutic strategies, Nat. Med. 23 (2017) 1–13. doi:10.1038/nm.4269.

[3] J. Hardy, D.J. Selkoe, The amyloid hypothesis of Alzheimer's disease: progress and problems on the road to therapeutics., Science. 297 (2002) 353–356. doi:10.1126/science.1072994.

[4] P. Calissano, C. Matrone, G. Amadoro, Apoptosis and in vitro Alzheimer's disease neuronal models, Commun. Integr. Biol. 2 (2009) 163–169. doi:10.4161/cib.7704.

[5] N. Canu, P. Calissano, In vitro cultured neurons for molecular studies correlating apoptosis with events related to Alzheimer disease, Cerebellum. 2 (2003) 270–278. doi:10.1080/14734220310004289.

[6] S. Shimohama, Apoptosis in Alzheimer's disease—an update, APOPTOSIS. 5 (2000) 9–16. doi:10.1023/A:1009625323388.

[7] W. Huang, X. Zhang, W. Chen, Role of oxidative stress in Alzheimer's disease (Review), Spandidos Publications, 2016. doi:10.3892/br.2016.630.

[8] F. Li, Q. Gong, H. Dong, J. Shi, Resveratrol, a neuroprotective supplement for Alzheimer's disease., Curr. Pharm. Des. 18 (2012) 27–33. http://www.ncbi.nlm.nih.gov/pubmed/22211686 (accessed October 23, 2017).

[9] W. Danysz, C.G. Parsons, Alzheimer's disease, β-amyloid, glutamate, NMDA receptors and memantine - searching for the connections, Br. J. Pharmacol. 167 (2012) 324–352. doi:10.1111/j.1476-5381.2012.02057.x.

[10] A.J. Doig, M.P. del Castillo-Frias, O. Berthoumieu, B. Tarus, J. Nasica-Labouze, F. Sterpone,

P.H. Nguyen, N.M. Hooper, P. Faller, P. Derreumaux, Why Is Research on Amyloid-β Failing to Give New Drugs for Alzheimer's Disease?, ACS Chem. Neurosci. 8 (2017) 1435–1437. doi:10.1021/acschemneuro.7b00188.

[11] P.C. Ke, M.-A. Sani, F. Ding, A. Kakinen, I. Javed, F. Separovic, T.P. Davis, R. Mezzenga, Implications of peptide assemblies in amyloid diseases, Chem. Soc. Rev. 46 (2017) 6492–6531. doi:10.1039/C7CS00372B.

[12] W.-J. Du, J.-J. Guo, M.-T. Gao, S.-Q. Hu, X.-Y. Dong, Y.-F. Han, F.-F. Liu, S. Jiang, Y. Sun, Brazilin inhibits amyloid β-protein fibrillogenesis, remodels amyloid fibrils and reduces amyloid cytotoxicity, Sci. Rep. 5 (2015) 7992. doi:10.1038/srep07992.

[13] J. Kim, H.J. Lee, K.W. Lee, Naturally occurring phytochemicals for the prevention of Alzheimer's disease, J. Neurochem. 112 (2010) 1415–1430. doi:10.1111/j.1471-4159.2009.06562.x.

[14] J. Zhao, Q. Liang, Q. Sun, C. Chen, L. Xu, Y. Ding, P. Zhou, (−)-Epigallocatechin-3-gallate (EGCG) inhibits fibrillation, disaggregates amyloid fibrils of α-synuclein, and protects PC12 cells against α-synuclein-induced toxicity, RSC Adv. 7 (2017) 32508–32517. doi:10.1039/C7RA03752J.

[15] P.H. Reddy, M. Manczak, X. Yin, M.C. Grady, A. Mitchell, S. Tonk, C.S. Kuruva, J.S. Bhatti, R. Kandimalla, M. Vijayan, S. Kumar, R. Wang, J.A. Pradeepkiran, G. Ogunmokun, K. Thamarai, K. Quesada, A. Boles, A.P. Reddy, Protective Effects of Indian Spice Curcumin Against Amyloid-β in Alzheimer's Disease., J. Alzheimers. Dis. 61 (2018) 843–866. doi:10.3233/JAD-170512.

[16] A.A. Reinke, J.E. Gestwicki, Structure-activity Relationships of Amyloid Beta-aggregation Inhibitors Based on Curcumin: Influence of Linker Length and Flexibility, Chem. Biol. Drug Des. 70 (2007) 206–215. doi:10.1111/j.1747-0285.2007.00557.x.

[17] S.-Y. Chen, Y. Chen, Y.-P. Li, S.-H. Chen, J.-H. Tan, T.-M. Ou, L.-Q. Gu, Z.-S. Huang, Design, synthesis, and biological evaluation of curcumin analogues as multifunctional agents for the treatment of Alzheimer's disease, Bioorg. Med. Chem. 19 (2011) 5596–5604. doi:10.1016/J.BMC.2011.07.033.

[18] C.I. Stains, K. Mondal, I. Ghosh, Molecules that Target beta-Amyloid, ChemMedChem. 2 (2007) 1674–1692. doi:10.1002/cmdc.200700140.

[19] F.H. Fahey, A.B. Goodkind, D. Plyku, K. Khamwan, S.E. O'Reilly, X. Cao, E.C. Frey, Y. Li, W.E. Bolch, G. Sgouros, S.T. Treves, Dose Estimation in Pediatric Nuclear Medicine, Semin. Nucl. Med. 47 (2017) 118–125. doi:10.1053/j.semnuclmed.2016.10.006.

[20] J. Nasica-Labouze, P.H. Nguyen, F. Sterpone, O. Berthoumieu, N.V. Buchete, S. Coté, A. De

Simone, A.J. Doig, P. Faller, A. Garcia, A. Laio, M.S. Li, S. Melchionna, N. Mousseau, Y. Mu, A. Paravastu, S. Pasquali, D.J. Rosenman, B. Strodel, B. Tarus, J.H. Viles, T. Zhang, C. Wang, P. Derreumaux, Amyloid β Protein and Alzheimer's Disease: When Computer Simulations Complement Experimental Studies, Chem. Rev. (2015). doi:10.1021/cr500638n.

[21] A.J. Doig, P. Derreumaux, Inhibition of protein aggregation and amyloid formation by small molecules, Curr. Opin. Struct. Biol. 30 (2015) 50–56. doi:10.1016/J.SBI.2014.12.004.

[22] J.A. Lemkul, D.R. Bevan, The Role of Molecular Simulations in the Development of Inhibitors of Amyloid β-Peptide Aggregation for the Treatment of Alzheimer's Disease, ACS Chem. Neurosci. 3 (2012) 845–856. doi:10.1021/cn300091a.

[23] P.H. Nguyen, M.P. Del Castillo-Frias, O. Berthoumieux, P. Faller, A.J. Doig, P. Derreumaux, Amyloid-β/Drug Interactions from Computer Simulations and Cell-Based Assays., J. Alzheimers. Dis. 64 (2018) S659–S672. doi:10.3233/JAD-179902.

[24] Y. Chebaro, P. Jiang, T. Zang, Y. Mu, P.H. Nguyen, N. Mousseau, P. Derreumaux, Structures of Aβ17–42 Trimers in Isolation and with Five Small-Molecule Drugs Using a Hierarchical Computational Procedure, J. Phys. Chem. B. 116 (2012) 8412–8422. doi:10.1021/jp2118778.

[25] P.P.N. Rao, T. Mohamed, K. Teckwani, G. Tin, Curcumin Binding to Beta Amyloid: A Computational Study, Chem. Biol. Drug Des. 86 (2015) 813–820. doi:10.1111/cbdd.12552.

[26] H.S. Kundaikar, M.S. Degani, Insights into the Interaction Mechanism of Ligands with A β 42 Based on Molecular Dynamics Simulations and Mechanics: Implications of Role of Common Binding Site in Drug Design for Alzheimer's Disease, Chem. Biol. Drug Des. 86 (2015) 805–812. doi:10.1111/cbdd.12555.

[27] A. Battisti, A. Palumbo Piccionello, A. Sgarbossa, S. Vilasi, C. Ricci, F. Ghetti, F. Spinozzi, A. Marino Gammazza, V. Giacalone, A. Martorana, A. Lauria, C. Ferrero, D. Bulone, M.R. Mangione, P.L. San Biagio, M.G. Ortore, B. Schmidt, Curcumin-like compounds designed to modify amyloid beta peptide aggregation patterns, RSC Adv. 7 (2017) 31714–31724. doi:10.1039/C7RA05300B.

[28] S.T. Ngo, M.S. Li, Curcumin binds to Aβ1-40 peptides and fibrils stronger than ibuprofen and naproxen, J. Phys. Chem. B. 116 (2012) 10165–10175. doi:10.1021/jp302506a.

[29] S.T. Ngo, S.-T. Fang, S.-H. Huang, C.-L. Chou, P.D.Q. Huy, M.S. Li, Y.-C. Chen, Anti-arrhythmic Medication Propafenone a Potential Drug for Alzheimer's Disease Inhibiting Aggregation of Aβ: In Silico and in Vitro Studies, J. Chem. Inf. Model. 56 (2016) 1344–1356. doi:10.1021/acs.jcim.6b00029.

[30] M. Awasthi, S. Singh, V.P. Pandey, U.N. Dwivedi, Modulation in the conformational and stability attributes of the Alzheimer's disease associated amyloid-beta mutants and their

favorable stabilization by curcumin: molecular dynamics simulation analysis., J. Biomol. Struct. Dyn. (2017) 1–16. doi:10.1080/07391102.2017.1279078.

[31] K.M. Nelson, J.L. Dahlin, J. Bisson, J. Graham, G.F. Pauli, M.A. Walters, The Essential Medicinal Chemistry of Curcumin, J. Med. Chem. 60 (2017) 1620–1637. doi:10.1021/acs.jmedchem.6b00975.

[32] J. Yan, J. Hu, A. Liu, L. He, X. Li, H. Wei, Design, synthesis, and evaluation of multitarget-directed ligands against Alzheimer's disease based on the fusion of donepezil and curcumin, Bioorg. Med. Chem. 25 (2017) 2946–2955. doi:10.1016/J.BMC.2017.02.048.

[33] A. Battisti, A. Palumbo Piccionello, A. Sgarbossa, S. Vilasi, C. Ricci, F. Ghetti, F. Spinozzi, A. Marino Gammazza, V. Giacalone, A. Martorana, A. Lauria, C. Ferrero, D. Bulone, M.R. Mangione, P.L. San Biagio, M.G. Ortore, Curcumin-like compounds designed to modify amyloid beta peptide aggregation patterns, RSC Adv. 7 (2017) 31714–31724. doi:10.1039/C7RA05300B.

[34] E. Ferrari, F. Pignedoli, C. Imbriano, G. Marverti, V. Basile, E. Venturi, M. Saladini, Newly Synthesized Curcumin Derivatives: Crosstalk between Chemico-physical Properties and Biological Activity, J. Med. Chem. 54 (2011) 8066–8077. doi:10.1021/jm200872q.

[35] H.J.J. Pabon, A synthesis of curcumin and related compounds, Recl. Des Trav. Chim. Des Pays-Bas. 83 (2010) 379–386. doi:10.1002/recl.19640830407.

[36] E. Ferrari, F. Pignedoli, C. Imbriano, G. Marverti, V. Basile, E. Venturi, M. Saladini, Newly synthesized curcumin derivatives: Crosstalk between chemico-physical properties and biological activity, J. Med. Chem. 54 (2011) 8066–8077. doi:10.1021/jm200872q.

[37] E. Ferrari, M. Asti, R. Benassi, F. Pignedoli, M. Saladini, Metal binding ability of curcumin derivatives: a theoretical vs. experimental approach, Dalt. Trans. 42 (2013) 5304. doi:10.1039/c3dt33072a.

[38] E. Ferrari, R. Benassi, S. Sacchi, F. Pignedoli, M. Asti, M. Saladini, Curcumin derivatives as metal-chelating agents with potential multifunctional activity for pharmaceutical applications, J. Inorg. Biochem. 139 (2014) 38–48. doi:10.1016/J.JINORGBIO.2014.06.002.

[39] P. Gans, A. Sabatini, A. Vacca, Investigation of equilibria in solution. Determination of equilibrium constants with the HYPERQUAD suite of programs, Talanta. 43 (1996) 1739–1753. doi:10.1016/0039-9140(96)01958-3.

[40] P. Gans, A. Sabatini, A. Vacca, To improve accuracy of the calculated pKa values, Ann. Chim. 89 (1999) 45–49.

[41] L. Rigamonti, G. Orteca, M. Asti, V. Basile, carol imbriano, M. Saladini, E. Ferrari, New curcumin-derived ligands and their affinity towards Ga3+, Fe3+ and Cu2+: spectroscopic

studies on complex formation and stability in solution, New J. Chem. (2018). doi:10.1039/C8NJ00535D.

[42] M. Asti, E. Ferrari, S. Croci, G. Atti, S. Rubagotti, M. Iori, P.C. Capponi, A. Zerbini, M. Saladini, A. Versari, Synthesis and Characterization of ^{68} Ga-Labeled Curcumin and Curcuminoid Complexes as Potential Radiotracers for Imaging of Cancer and Alzheimer's Disease, Inorg. Chem. 53 (2014) 4922–4933. doi:10.1021/ic403113z.

[43] S. Rubagotti, S. Croci, E. Ferrari, M. Iori, P. Capponi, L. Lorenzini, L. Calzà, A. Versari, M. Asti, Affinity of nat/68Ga-Labelled Curcumin and Curcuminoid Complexes for β-Amyloid Plaques: Towards the Development of New Metal-Curcumin Based Radiotracers, Int. J. Mol. Sci. 17 (2016) 1480. doi:10.3390/ijms17091480.

[44] N. Homeyer, H. Gohlke, Free energy calculations by the Molecular Mechanics Poisson-Boltzmann Surface Area method, Mol. Inform. 31 (2012) 114–122. doi:10.1002/minf.201100135.

[45] Y. Masuda, M. Fukuchi, T. Yatagawa, M. Tada, K. Takeda, K. Irie, K.-I. Akagi, Y. Monobe, T. Imazawa, K. Takegoshi, Solid-state NMR analysis of interaction sites of curcumin and 42-residue amyloid β-protein fibrils, Bioorg. Med. Chem. 19 (2011) 5967–5974. doi:10.1016/j.bmc.2011.08.052.

[46] M. Friedemann, E. Helk, A. Tiiman, K. Zovo, P. Palumaa, V. Tõugu, Effect of methionine-35 oxidation on the aggregation of amyloid-β peptide, Biochem. Biophys. Reports. 3 (2015) 94–99. doi:10.1016/j.bbrep.2015.07.017.

[47] W. Qiang, W.-M. Yau, Y. Luo, M.P. Mattson, R. Tycko, Antiparallel β-sheet architecture in Iowa-mutant β-amyloid fibrils, Proc. Natl. Acad. Sci. 109 (2012) 4443–4448. doi:10.1073/pnas.1111305109.

[48] W.M. Berhanu, U.H.E. Hansmann, Structure and Dynamics of Amyloid-β Segmental Polymorphisms, PLoS One. 7 (2012) e41479. doi:10.1371/journal.pone.0041479.

[49] M. Awasthi, S. Singh, V.P. Pandey, U.N. Dwivedi, Modulation in the conformational and stability attributes of the Alzheimer's disease associated amyloid-beta mutants and their favorable stabilization by curcumin: molecular dynamics simulation analysis, J. Biomol. Struct. Dyn. (2017) 1–16. doi:10.1080/07391102.2017.1279078.

[50] A.A. Kritis, E.G. Stamoula, K.A. Paniskaki, T.D. Vavilis, Researching glutamate â€“ induced cytotoxicity in different cell lines: a comparative/collective analysis/study, Front. Cell. Neurosci. 9 (2015) 91. doi:10.3389/fncel.2015.00091.

[51] M. Fukui, J.-H. Song, J. Choi, H.J. Choi, B.T. Zhu, Molecular and Cellular Pharmacology Mechanism of glutamate-induced neurotoxicity in HT22 mouse hippocampal cells, (2009).

doi:10.1016/j.ejphar.2009.06.059.
[52] M. Borsari, E. Ferrari, R. Grandi, M. Saladini, Curcuminoids as potential new iron-chelating agents: spectroscopic, polarographic and potentiometric study on their Fe(III) complexing ability, Inorganica Chim. Acta. 328 (2002) 61–68. doi:10.1016/S0020-1693(01)00687-9.
[53] V. Basile, E. Ferrari, S. Lazzari, S. Belluti, F. Pignedoli, C. Imbriano, Curcumin derivatives: Molecular basis of their anti-cancer activity, Biochem. Pharmacol. 78 (2009) 1305–1315. doi:10.1016/J.BCP.2009.06.105.
[54] A. Koeberle, E. Muñoz, G.B. Appendino, A. Minassi, S. Pace, A. Rossi, C. Weinigel, D. Barz, L. Sautebin, D. Caprioglio, J.A. Collado, O. Werz, SAR studies on curcumin's pro-inflammatory targets: Discovery of prenylated pyrazolocurcuminoids as potent and selective novel inhibitors of 5-lipoxygenase, J. Med. Chem. 57 (2014) 5638–5648. doi:10.1021/jm500308c.
[55] P. Cornago, R.M. Claramunt, L. Bouissane, I. Alkorta, J. Elguero, A study of the tautomerism of β-dicarbonyl compounds with special emphasis on curcuminoids, Tetrahedron. 64 (2008) 8089–8094. doi:10.1016/J.TET.2008.06.065.
[56] R.M. Claramunt, L. Bouissane, M.P. Cabildo, M.P. Cornago, J. Elguero, A. Radziwon, C. Medina, Synthesis and biological evaluation of curcuminoid pyrazoles as new therapeutic agents in inflammatory bowel disease: Effect on matrix metalloproteinases, Bioorg. Med. Chem. 17 (2009) 1290–1296. doi:10.1016/J.BMC.2008.12.029.
[57] S. Pronk, S. Páll, R. Schulz, P. Larsson, P. Bjelkmar, R. Apostolov, M.R. Shirts, J.C. Smith, P.M. Kasson, D. van der Spoel, B. Hess, E. Lindahl, GROMACS 4.5: a high-throughput and highly parallel open source molecular simulation toolkit, Bioinformatics. 29 (2013) 845–854. doi:10.1093/bioinformatics/btt055.
[58] A.K. Malde, L. Zuo, M. Breeze, M. Stroet, D. Poger, P.C. Nair, C. Oostenbrink, A.E. Mark, An Automated Force Field Topology Builder (ATB) and Repository: Version 1.0, J. Chem. Theory Comput. 7 (2011) 4026–4037. doi:10.1021/ct200196m.
[59] K.B. Koziara, M. Stroet, A.K. Malde, A.E. Mark, Testing and validation of the Automated Topology Builder (ATB) version 2.0: prediction of hydration free enthalpies, J. Comput. Aided. Mol. Des. 28 (2014) 221–233. doi:10.1007/s10822-014-9713-7.
[60] A.K. Paravastu, R.D. Leapman, W.-M. Yau, R. Tycko, Molecular structural basis for polymorphism in Alzheimer's β-amyloid fibrils, Proc. Natl. Acad. Sci. 105 (2008) 18349–18354. doi:10.1073/pnas.0806270105.
[61] W. Humphrey, A. Dalke, K. Schulten, VMD: visual molecular dynamics, J. Mol. Graph. 14 (1996) 33–38, 27–28.

[62] A. Drozdetskiy, C. Cole, J. Procter, G.J. Barton, JPred4: a protein secondary structure prediction server, Nucleic Acids Res. 43 (2015) W389–W394. doi:10.1093/nar/gkv332.
[63] N. Eswar, B. Webb, M.A. Marti-Renom, M.S. Madhusudhan, D. Eramian, M.-Y. Shen, U. Pieper, A. Sali, Comparative protein structure modeling using Modeller, Curr. Protoc. Bioinforma. Chapter 5 (2006) Unit 5.6. doi:10.1002/0471250953.bi0506s15.
[64] G.M. Morris, R. Huey, W. Lindstrom, M.F. Sanner, R.K. Belew, D.S. Goodsell, A.J. Olson, AutoDock4 and AutoDockTools4: Automated docking with selective receptor flexibility, J. Comput. Chem. 30 (2009) 2785–2791. doi:10.1002/jcc.21256.
[65] N. Schmid, A.P. Eichenberger, A. Choutko, S. Riniker, M. Winger, A.E. Mark, W.F. van Gunsteren, Definition and testing of the GROMOS force-field versions 54A7 and 54B7, Eur. Biophys. J. EBJ. 40 (2011) 843–856. doi:10.1007/s00249-011-0700-9.
[66] P. Robustelli, S. Piana, D.E. Shaw, Developing a molecular dynamics force field for both folded and disordered protein states., Proc. Natl. Acad. Sci. U. S. A. 115 (2018) E4758–E4766. doi:10.1073/pnas.1800690115.
[67] F. Tavanti, A. Pedone, M. Menziani, Computational Insight into the Effect of Natural Compounds on the Destabilization of Preformed Amyloid-β(1–40) Fibrils, Molecules. 23 (2018) 1320. doi:10.3390/molecules23061320.
[68] H.J.C. Berendsen, J.P.M. Postma, W.F. van Gunsteren, J. Hermans, Interaction Models for Water in Relation to Protein Hydration, in: B. Pullman (Ed.), Intermol. Forces, Springer Netherlands, 1981: pp. 331–342.
[69] T. Darden, D. York, L. Pedersen, Particle mesh Ewald: An N·log(N) method for Ewald sums in large systems, J. Chem. Phys. 98 (1993) 10089–10092. doi:10.1063/1.464397.
[70] U. Essmann, L. Perera, M.L. Berkowitz, T. Darden, H. Lee, L.G. Pedersen, A smooth particle mesh Ewald method, J. Chem. Phys. 103 (1995) 8577–8593. doi:10.1063/1.470117.
[71] GROMACS: High performance molecular simulations through multi-level parallelism from laptops to supercomputers, GROMACS User Man. Version 5.0.4. (n.d.).
[72] R. Kumari, R. Kumar, A. Lynn, g_mmpbsa—A GROMACS Tool for High-Throughput MM-PBSA Calculations, J. Chem. Inf. Model. 54 (2014) 1951–1962. doi:10.1021/ci500020m.
[73] V. Basile, F. Baruffaldi, D. Dolfini, S. Belluti, P. Benatti, L. Ricci, V. Artusi, E. Tagliafico, R. Mantovani, S. Molinari, C. Imbriano, NF-YA splice variants have different roles on muscle differentiation, Biochim. Biophys. Acta - Gene Regul. Mech. 1859 (2016) 627–638. doi:10.1016/j.bbagrm.2016.02.011.